The Thesis committee for Rik Dey

Certifies that this is the approved version of the following thesis:

Perpendicular And Parallel Field Magnetoresistance In Molecular Beam Epitaxy Grown Bi_2Te_3

APPROVED BY
SUPERVISING COMMITTEE:

Supervisor: _____

Sanjay Kumar Banerjee

_____

Leonard Franklin Register

Perpendicular And Parallel Field Magnetoresistance In Molecular Beam Epitaxy Grown Bi_2Te_3

by

Rik Dey, B. Tech.

Thesis

Presented to the Faculty of the Graduate School

of the University of Texas at Austin

in Partial Fulfillment

of the Requirements

for the Degree of

Master of Science in Engineering

The University of Texas at Austin

August 2014

Acknowledgments

I would like to thank my supervisor Prof. Sanjay Kumar Banerjee, for giving me the great opportunity to work in his group. He gave me the chance to develop new skills, gather useful knowledge and experiences, while allowing me to work in my own way. I sincerely thank him for supporting me throughout my research.

I express my deepest gratitude to Prof. Leonard Franklin Register for his invaluable suggestions on my research and for serving as the reader for my thesis. He supported me throughout my research with his patience and knowledge. Many thanks to Luigi Colombo for his advice during the Monday meetings.

Special thanks goes to Dr. Anupam Roy for his work on the growth and the surface characterization part. I have learned a lot about the growth and the characterization techniques from him. My sincere thanks to Dr. Samaresh Guchhait and Dr. Sushant Shonde for helping me in other experimental tools.

I would like to specially thank my group members Tanmoy for helping me in the coding part, and Hema for helping me writing this thesis. I am grateful to them, and to my other colleagues Amritesh, Tanuj, Urmimala, Amith and Dax for many useful discussions and conversations.

My sincere appreciation goes to the MER staff Jeannie, Ricardo, Johnny and Jesse for their continuous help and support.

I would also like to thank Saugata for the occasional Saturday night parties and having lots of fun. Thanks goes to my group members again for those weekend parties and movies. Thanks a lot to my wing mates for the overseas video calls and messages.

I would like to thank my parents and my extended family. This thesis would not have been possible without the unconditional love and support from my parents. Thanks a lot to my *Ma* and *Baba* for believing in me and sacrificing a lot for me.

Abstract

Perpendicular And Parallel Field Magnetoresistance In Molecular Beam Epitaxy Grown Bi_2Te_3

by

Rik Dey, M. S. E.

The University of Texas at Austin, 2014

SUPERVISOR: Sanjay Kumar Banerjee

The topological insulator Bi_2Te_3 has been grown on Si(111)-(7 $\times$ 7) surface by molecular beam epitaxy. Reflection high energy electron diffraction, in situ scanning tunnelling microscopy, x-ray photoelectron spectroscopy and ex situ x-ray diffraction studies have been performed to analyze the quality of the growth. These analyses suggest a very good layer-by-layer epitaxial growth of Bi_2Te_3 on the atomically flat Si surface. The magnetoresistance of the samples has been studied with magnetic field perpendicular and parallel to the sample surface, up to 9 T, over a temperature range of 2 K to 20 K. A sharp dip at low fields (0 T $-$ 1 T) and near-linear behavior for high fields ($>$ 4 T) have been observed in the perpendicular field magnetoresistance. The low field dip is due to weak antilocalization that agrees well with the simplified Hikami-Larkin-Nagaoka model. It has been demonstrated that both the low field dip and the high field near-linear behavior can be explained by the original Hikami-Larkin-Nagaoka formula alone in a system with strong spin-orbit coupling. From the fitting of the perpendicular field magnetoresistance the phase coherence length, the mean free path and the spin-orbit relaxation time have been estimated. The phase coherence length shows power law dependence with temperature indicating two dimensional nature of the transport. The power law also suggests electron electron interaction as

the prominent dephasing mechanism. The out-of-plane spin-orbit relaxation time is determined to be small and the in-plane spin-orbit relaxation time is found to be comparable to the momentum relaxation time. The estimation of these charge and spin transport parameters is useful for topological insulator based magneto electric device applications. It also has been shown that the strong spin-orbit coupling suppresses the Zeeman contribution in perpendicular field magnetoresistance. The logarithmic divergence of perpendicular field magnetoresistance with temperature for low temperature range (2 K $-$ 20 K) at high fields shows the presence of Coulomb interaction in the spin singlet channel. For magnetoresistance with the field parallel to the sample surface, the observed magnetoresistance has parabolic dependence for small fields (0 T $-$ 0.6 T) and logarithmic dependence for large fields ($>$ 3 T), which is due to the Zeeman effect. It is found that the data are inconsistent with only the Maekawa and Fukuyama theory of non interacting electrons with Zeeman contributions to the transport, but are consistent with theory if one also takes into account the electron electron interaction and the Zeeman splitting term in the electron electron interaction theory of Lee and Ramakrishnan. The Zeeman g-factor and the strength of Coulomb scattering due to electron electron interaction have been estimated from fitting of the parallel field magnetoresistance. The magnetoresistance also shows anisotropy with respect to the field directions. The angle dependent anisotropic magnetoresistance can be fitted well by the original HLN theory alone. The anisotropy can have potential application in anisotropic magnetic sensors.

Contents

List of Figures

1

Introduction

1.1 Topological Insulators: Overview

Topological insulators (TIs) are exciting novel materials exhibiting unique quantum-mechanical properties and have gained considerable attention in recent research in condensed matter physics. Band theory divides solids into metals and insulators: metals are those with no band gap and insulators have a non-zero band gap. TIs are unique in having a gaped bulk and gapless surface states with a well-defined spin texture [1, 2, 3, 4, 5, 6, 7, 8, 9]. The surface states have a Dirac cone dispersion relation and the spin of the Dirac fermions are perpendicularly locked to the momentum. Such property of the TIs are very useful in spintronics applications where manipulation of the spin current by the charge transport is a central aim. The study of TIs is also motivated by theoretical prediction of many exotic phenomenon such as existence of Majorana fermions in close proximity of a superconductor and existence of magnetic monopoles [10, 11].

1.2 Topological Insulators: Properties

Most of the exotic and unique quantum-mechanical properties of TIs are a direct consequence of the band structure of the edge states of two dimensional (2D) TIs or the surface states of three dimensional (3D) TIs. The fermions in the edge states or in the surface states behave like relativistic, mass-less particles around the Dirac point with spin-momentum helical locking. This peculiar nature of the Dirac fermions in a TI gives rise to potential novel application of TI materials in spintronics, magnetic sensors and memory devices [2, 3, 4, 5, 6, 7, 12, 13, 14, 15].

1.2.1 Schematic band structure of TIs

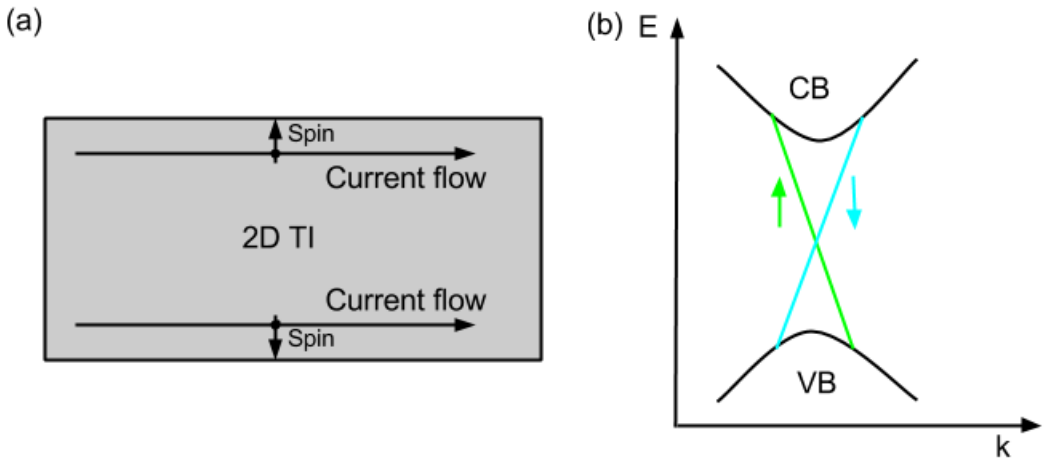

Figure 1.1: Edge states of a 2D TI: (a) 1D edge state of a 2D TI in real-space, (b) 1D Dirac cone dispersion relation represnting the edge states.

Figure 1.1 shows edge states of a 2D TI and Figure 1.2 shows surface states of a 3D TI, both having a Dirac dispersion relation with spin-momentum locking. Figure 1.1(a) and Figure 1.2(a) show a schematic of real-space picture of one dimensional edge states in a 2D TI and 2D surface states in a 3D TI respectively. Figure 1.1(b)

and Figure 1.2(b) correspondingly show the band structure of a 2D and 3D TI, respectively. The spin and momentum are helically locked in the 2D surface states of a 3D TI, which is shown in Figure 1.2(b). The spin-momentum helical locking is protected by time-reversal symmetry (TRS). Only magnetic perturbation can break the TRS and induce gap in the surface states of TI. Due to the helical spin polarization, back scattering is also prohibited in the surface states.

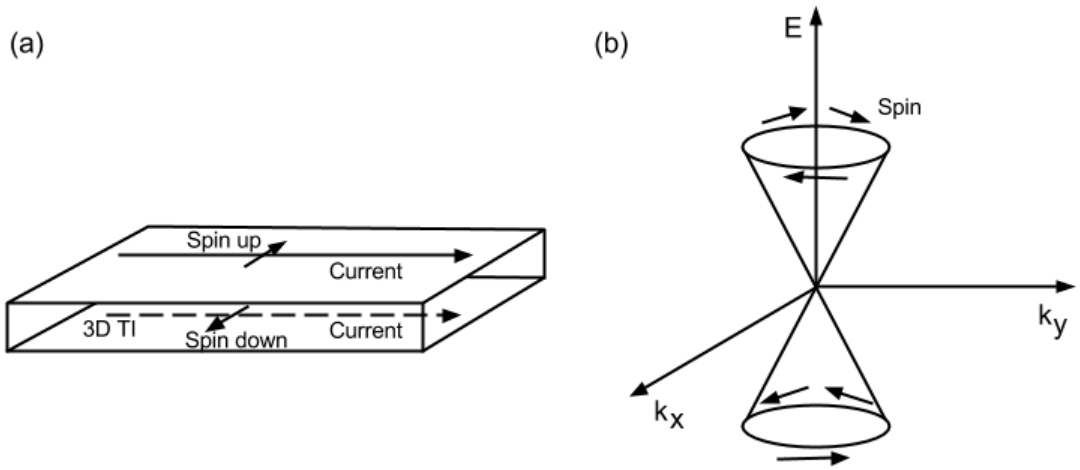

Figure 1.2: Surface states of a 3D TI: (a) 2D surface state of a 3D TI in real-space, (b) 2D Dirac cone dispersion relation representing the surface states.

The existence of metallic surface states has been theoretically predicted and experimentally verified in Bi_2Se_3, Bi_2Te_3, Sb_2Te_3 and many more [6, 7, 8, 9]. These materials have strong spin-orbit coupling (SOC) due to the heavy metal element. These materials have been long known for their thermoelectric behavior and well studied [16]. The existence of surface states has renewed interest in synthesizing and characterizing such materials.

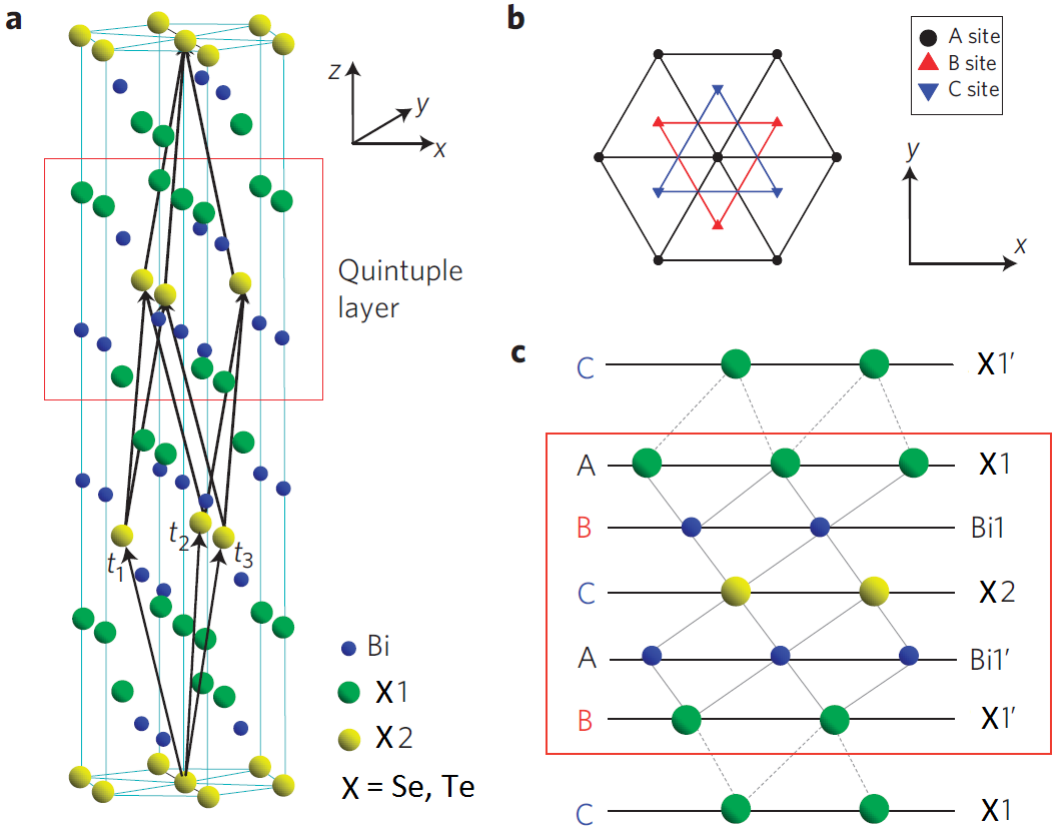

Figure 1.3: Crystal structure of Bi_2X_3 (X = Se, Te) showing quintuple layer (taken from [7]): (a) Three primitive lattice vectors $t_{1,2,3}$ and a QL are shown, (b) Top view of the crystal, (c) Side view of the crystal.

1.2.2 Crystal structure of Bi_2Se_3 and Bi_2Te_3

Bi_2Se_3 and Bi_2Te_3 both crystallize in tetradynamite structure (rhombohedral crystal structure consisting of 5-atom unit cell) belonging to the $D^5_{3d}(R\bar{3}m)$ space group [7]. The crystal has 3-fold rotational symmetry along the z axis, 2-fold rotational symmetry along the x axis and a yz reflection plane. Figure 1.3 shows the crystal structure of Bi_2X_3 (X=Se, Te) with the three primitive lattice vectors and the quintuple layer (QL). A QL is the primitive unit cell thickness consisting of five atomic layers. In a QL (X-Bi-X-Bi-X), there are two equivalent Bi atoms Bi1 and Bi1′, two equivalent X atoms X1 and X1′ and a third X atom X2 as shown in Figure 1.3(a). The QLs

are stacked in A-B-C-A-B-C- manner, with the atomic positions A, B, C as shown in Figure 1.3(b). The third X atom X2 is the inversion center for the inversion operation by which Bi1 goes to Bi1′ and X1 goes to X1′. Existence of inversion symmetry allows eigenstates of the system to have definite parity. The other important symmetry of the system is the TRS. The material is a layered material as the couplings between atoms of two neighboring QLs are van-der Waals interactions, but within Ql the interactions between the atoms are stronger to hold the atoms together in a QL. The side view of a QL is shown in Figure 1.3(c).

1.2.3 Band structure of Bi_2Se_3 and Bi_2Te_3

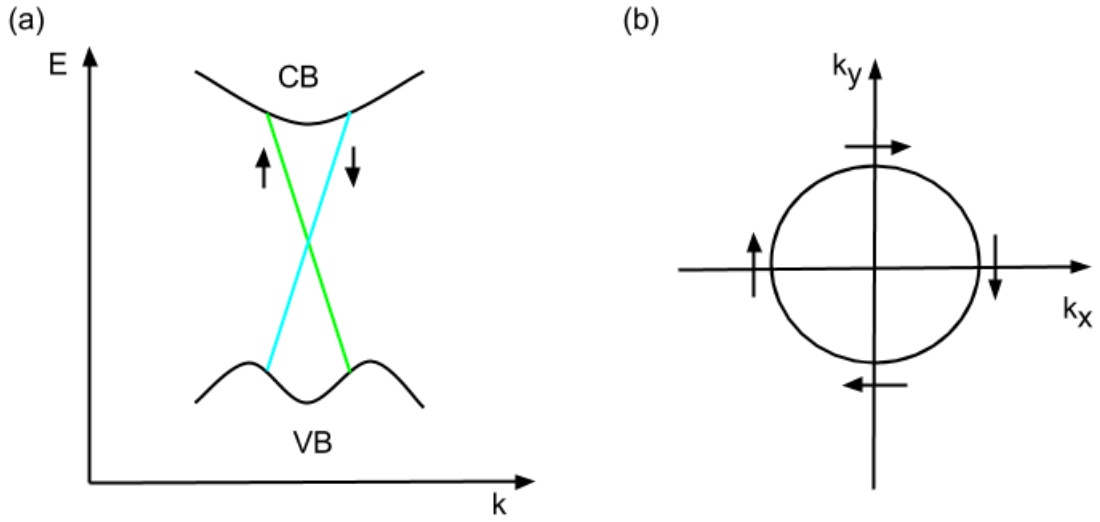

Figure 1.4: Schematic band structure of Bi_2Se_3 showing constant energy contour in the Dirac cone (adapted from [17]): (a) E-k diagram for Bi_2Se_3, (b) Constant energy surface for Bi_2Se_3 is almost spherical.

The topological surface state of these 3D Z_2 invariant tetradynamite structure are mainly centered around Γ point in reciprocal space. The complicated band structure can be simplified to an effective Hamiltonian of the system to characterize the low

energy and long wavelength excitations. The effective Hamiltonian can be written in the basis of the molecular p_z orbitals (atomic p_z orbitals of Bi and Se form molecular orbitals) closest in energy to the Fermi energy [7]. There are four spin-orbitals due to a two pairs of spin degenerate orbitals, one pair for the Bi atom and another pair for the Se atom. The 4×4 effective Hamiltonian matrix in this four orbital basis can be projected onto the subspace of the surface states which are the normalized solutions of the effective Hamiltonian in $z > 0$ half infinite space around the Γ point (i.e. $k_x = 0$ and $k_y = 0$ point). The Hamiltonian projected onto the subspace of surface states then reads as [7]:

$$H = E_0 + \hbar v_F (k_x \sigma_y - k_y \sigma_x). \tag{1.1}$$

Here $\hbar$ is the reduced Planck constant, E_0 is the energy of the Dirac point (reference of the energy), v_F is the Fermi velocity and σ_x, σ_y are the Dirac matrices. The Hamiltonian in Equation 1.1 represents a linear Dirac cone with spin-momentum helical locking between momentum and spin orientation. The dispersion relation is given by,

$$E(k) = E_0 + \hbar v_F k, \tag{1.2}$$

where $k = \sqrt{k_x^2 + k_y^2}$. For Bi_2Se_3, the actual Dirac cone is almost linear with slight curvature [7, 17] and the surface can be described by such a Hamiltonian given in Equation 1.1. The Dirac point also lies in the bulk band gap in the case of Bi_2Se_3, and the constant energy surface in the Dirac cone of Bi_2Se_3 is spherical, as shown in Figure 1.4(a) and Figure 1.4(b) respectively.

For Bi_2Te_3, the actual surface states are complicated and the Dirac point lies below the bulk valence band [17]. The constant energy surface in the Dirac cone of

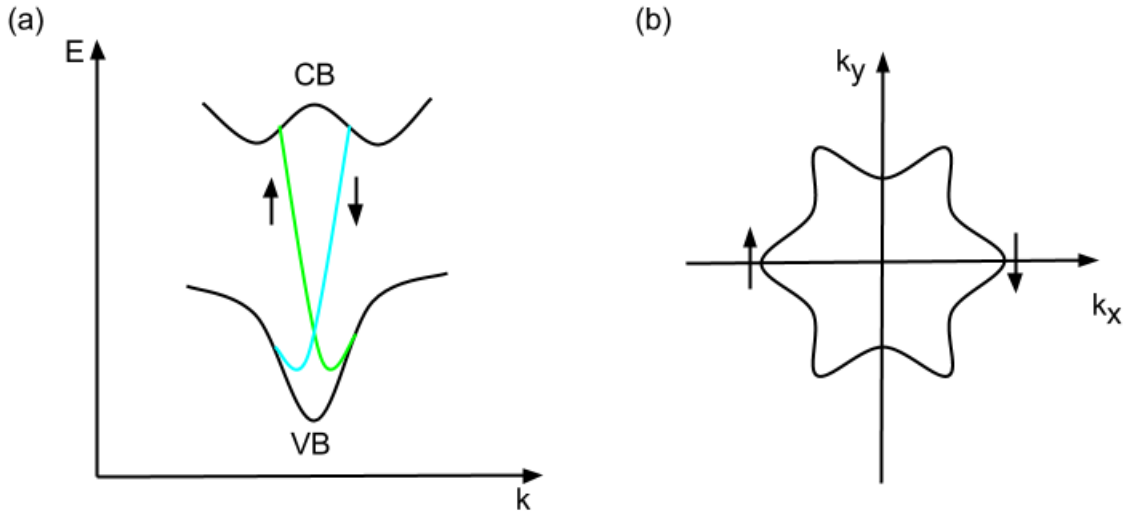

Figure 1.5: Schematic band structure of Bi_2Te_3 showing constant energy contour in the Dirac cone (adapted from [17]): (a) E-k diagram for Bi_2Te_3, (b) Constant energy surface for Bi_2Te_3 has hexagonal warping effect.

Bi_2Te_3 is not spherical and has hexagonal warping [13, 18] due to cubic Dresselhaus spin orbit coupling. The surface state Hamiltonian with hexagonal warping has the form [18]:

$$H = E_0 + \hbar v_F(1 + \alpha k^2)(k_x\sigma_y - k_y\sigma_x) + \frac{k^2}{2m^*} + \frac{\lambda}{2}(k_+^3 + k_-^3)\sigma_z, \tag{1.3}$$

where $k_\pm = k_x \pm k_y$, σ_z is the Dirac matrices, λ is the strength of Dresselhaus spin-orbit interaction and α, m^* are for higher order corrections. Figure 1.5(a) and Figure 1.5(b) shows the E-k diagram and the constant energy contour for Bi_2Te_3, respectively.

Gap opening in thin films

For an ultrathin film, the 3D TI reaches a 2D limit in which the two surfaces are coupled producing a energy gap Δ opening about what would otherwise be the Dirac point (i.e Γ point in k-space), and the nominally bulk states also become quasi-2D

[19, 20, 21, 22, 23, 24, 25]. The band structure of the TI in this limit depends on the layer thickness, i.e. the number of QLs. This 2D limit of TIs has been observed experimentally in Bi_2Se_3, Bi_2Te_3 by ARPES [21, 22, 23, 24, 25] and transport studies [26, 27]. The Hamiltonian for a gapped surface near the Dirac point with a energy gap opening Δ is given by [19],

$$H = E_0 + \hbar v_F(k_x\sigma_y - k_y\sigma_x) + \frac{\Delta}{2}\sigma_z. \tag{1.4}$$

The $E(k)$ relationship for a thin TI is approximately,

$$E(k) = E_0 + \sqrt{(\hbar v_F k)^2 + (\Delta/2)^2}. \tag{1.5}$$

The Berry phase of a normal linear Dirac surface state is equal to π, but for a gapped surface state the Berry phase changes to $\pi(1 - \Delta/2E_F)$ [19, 28] (where E_F is the Fermi energy). For a TI film as the thickness increases the gap vanishes, the Dirac cone remains linear around the Dirac point and the two surfaces become decoupled.

1.3 Topological Insulators: Synthesis

To study the properties of the surface states of TI, thin films of high purity with low defects are desirable. There are several methods including exfoliation from a bulk crystal grown by Bridgman method, or direct growth of thin film on a suitable substrate using chemical vapor deposition (CVD) or molecular beam epitaxy (MBE). As Bi_2Se_3 and Bi_2Te_3 are layered material, graphene like mechanical exfoliation of thin flakes from a bulk crystal is possible on a SiO_2/Si substrate [29, 30, 31]. The bulk crystal can be grown by Bridgman method [17]. In Bridgman method, the growth is done in a sealed evacuated quartz glass tube with a certain temperature gradient.

High purity source materials are evaporated at the hot end, and the crystal grows gradually once solidification of the compound material starts at the cold end. In MBE, source material are co-evaporated with a certain flux ratio to form the compound in a heated substrate. By MBE, growth of defect free high quality epitaxial thin films is possible on different substrate such as GaAs(001) [32], GaAs(111) [33], sapphire(0001) [34], $SrTiO_3$ [35], Si(111) [36, 37, 38, 24] etc. Thin films of Bi_2Se_3 have been grown by the CVD technique too [39, 40], but the film quality of MBE grown films are better than CVD grown films.

1.4 Topological Insulators: Transport

The quantum transport properties of the surface states of TIs also have been studied by various magneto-transport experiments such as Aharonov-Bohm oscillations [15, 41], Shubnikov-de Haas oscillations [42, 43], quantum conductance fluctuations [44, 45], and weak antilocalization (WAL) effects [46, 47, 48, 49, 50, 51, 52, 53, 54]. Although investigating transport in the surface states by such experiments is challenging because of significant bulk conduction, reduction of bulk conduction can be achieved by fabricating ultrathin TI films that increase the surface-to-volume ratio. If the bulk becomes sufficiently insulating and the Fermi level lies in the bulk band gap, then only the surface states will contribute to the transport. The nature of the surface state can be probed by sample-size dependent transport phenomenon, such as elucidating the π Berry phase in quantum oscillations in quantum Hall effect and/or in weak antilocalization measurement or by probing the spin-momentum helical locking. Such measurements also help to differentiate the contribution from the Dirac fermions and fermions in a trivial 2D gas accumulated at the surface.

1.4.1 Quantum Hall Effect

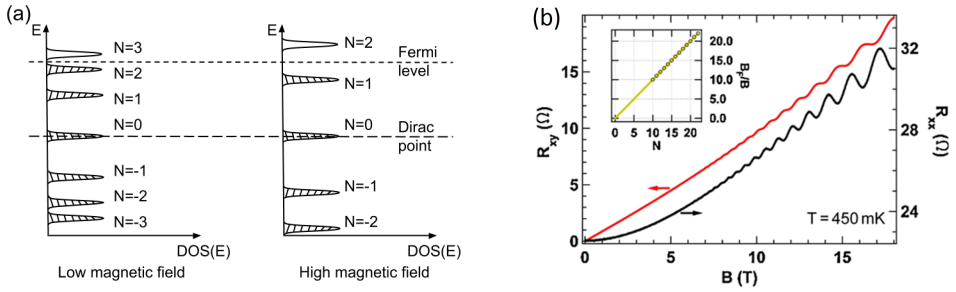

Figure 1.6: Quantum Hall Effect showing LL splitting and SdH oscillations: (a) LL splitting is shown at low and high magnetic field. Splitting is more at higher field. N is the LL index, where $N = 0$ is pinned at the Dirac point. (b) Oscillations in R_{xx} and R_{xy} in an applied magnetic field B is shown [55]. The inset shows B_F/B with N (where B_F is the associated oscillation frequency).

In an applied magnetic field, the energy states of the 2D system becomes quantized, which is called the Landau quantization and the discrete energy levels are called Landau Levels (LLs). Due to Landau quantization, the density of states (DOS) becomes periodically modulated with magnetic field. Oscillations occur in both the longitudinal resistance (R_{xx}) and the transverse resistance (R_{xy}), such oscillations are called Shubnikov-de Haas (SdH) oscillations. Figure 1.6(a) shows the effect of magnetic field on the LL splitting and DOS. Figure 1.6(b) shows the observed SdH oscillation in longitudinal resistance (R_{xx}) and transverse resistance (R_{xy}) in a Bi_2Se_3 film [55]. Such SdH oscillations help to differentiate transport quantitatively from the 2D surface states and the 3D bulk. Also the effect of π Berry phase is directly reflected on the phase factor of the SdH oscillations, which further differentiates transport from the fermions in a 2D Dirac cone and fermions in a trivial 2D Fermi gas. SdH oscillations have been observed experimentally in Bi_2Se_3 [55] and Bi_2Te_3 [42].

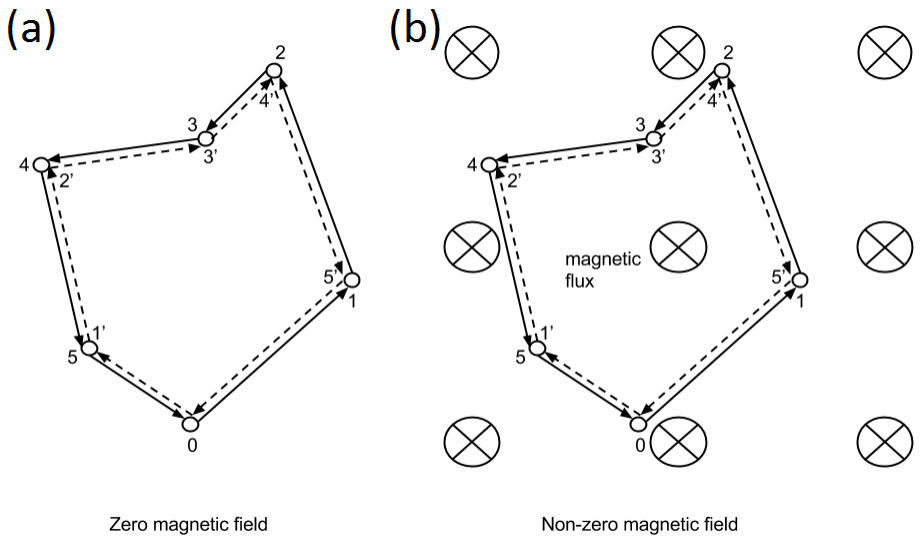

Figure 1.7: Weak localization in a normal metal without any magnetic field and suppression of weak localization in an applied field: (a) With no magnetic field applied: for each path that brings the particle back to origin, there is a time reversed path, and the two paths interfere constructively if TRS is preserved. (b) With non-zero magnetic field applied: The field breaks the TRS and there is phase difference between the two paths. The phase difference depends on the magnetic flux enclosed by the closed contour.

1.4.2 Weak Antilocalization Effect

Localization is a quantum mechanical phenomenon due to wave nature of electrons in a metallic material. In normal metals without spin orbit coupling, electronic wave functions between two time reversed path interfere constructively, enhancing the probability of finding an electron in a certain spatial position, as shown in Figure 1.7(a). In other words, the electron becomes localized in space. This localization effect reduces the probability of transmission of electrons, thus reduces the current and the resistance increases from the Drude resistance. This localization of electrons in a normal metal is called weak localization (WL). As shown in Figure 1.7(b), in an applied magnetic field the TRS is broken and the different time reversed paths acquire different phase factors in the electronic wave functions, which no longer interfere

constructively. Thus the probability of transmission increases and the resistance decreases. So application of a magnetic field destroys the localization effect and produce a negative magnetoresistance.

Weak antilocalization effect is just the opposite of weak localization, and in WAL the resistance without a magnetic field is less than the Drude resistance. The WAL effect associated with the Dirac fermions is due to an additional π (the π Berry phase) phase shift of the electronic wave functions along a closed loop [12, 49, 53, 56, 57, 58]. So destructive interference occurs between wave functions in the two time reversed path, which reduces the probability of localization and enhances the transmission or the current. This effect of reduced localization is called antilocalization. The resistance increases with application of a magnetic field as TRS is broken and destructive interference between the two paths is destroyed in a magnetic field. WAL can also occur in a strong SOC system, where the electrons acquire an additional phase π by scattering from impurity. Due to strong coupling of spin to momentum, the spin also changes as the momentum changes by scattering. Similar destructive interference occurs and antilocalization happens. In an applied magnetic field, the magnetoresistance is similarly postie. In case of TIs, if the Fermi energy lies deep in the bulk-state band structure due to unintentional doping, a WAL effect can still be observed in the topologically non-trivial 2D electron system as long as the SOC is strong enough [49, 53, 24, 59, 60]. Although a clear-cut separation of the two contributions is challenging, for both cases the observed WAL effect has a characteristic dip in low fields, which has been explained using simplified Hikami-Larkin-Nagaoka (HLN) theory under strong SOC and the low field limit [46, 47, 48, 49, 50, 51, 52, 53, 54, 61]

1.4.3 Electron Electron Interaction Effect

WAL in perpendicular field magnetoresistance of TI films has been widely reported in the literature [46, 47, 48, 49, 50, 51, 52, 53, 54, 61]. In the non-interacting electronic regime, WAL predicts a metallic ground state as the Dirac fermions can not be localized even in the presence of arbitrarily strong disorder [62, 63]. But the observation of an insulating ground state in resistance vs temperature plot of Bi_2Se_3 [50, 51] creates an interesting puzzle. Figure 1.8(a) shows the logarithmic divergence of resistance with temperature for Bi_2Se_3 of different thickness [50]. Figure 1.8(b) shows the logarithmic decreases of conductance with decrease of temperature for Bi_2Se_3 with a zero and non-zero magnetic field [51]. This puzzle can be resolved by considering the Coulomb interactions between the Dirac fermions. The Coulomb interaction is retarded and long ranged in a 2D diffusive system. Thus the electron electron interaction (EEI) is strong enough and can not be screened immediately. This EEI causes a reduction of density of states at the Fermi energy and a logarithmic divergence with temperature is observed in the resistivity.

1.4.4 Zeeman Effect

In a magnetic field, there is an additional energy called the Zeeman energy that is due to splitting of spin singlet and spin triplet channel. Zeeman spin splitting is also important in magnetoresistance of TIs and has been considered for Bi_2Se_3 [50, 51]. The contribution of the Zeeman energy is due both to the theory of localization and the theory of EEI. The HLN theory [64] does not consider the Zeeman energy, but the theory of Maekawa and Fukuyama [65] does consider the Zeeman spin splitting in localization of non-interacting electrons. Similarly, the theory of Lee and Ramakrishnan [66] for EEI takes care of the Zeeman term via the Hartree-Fock calculation.

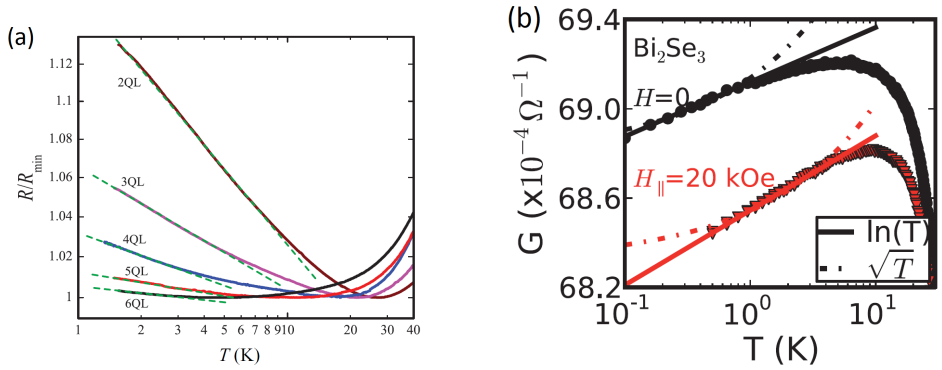

Figure 1.8: Observation of insulating ground state in Bi_2Se_3. (a) The resistance R increases with decreasing temperature. The resistance is fitted with a logarithmic dependence of temperature for different QL thickness (taken from [50]). (b) The conductance G decreases as the temperature decreases. The conductance is fitted with a logarithmic dependence with temperature for both cases, i.e. with and without a magnetic field (taken from [51]).

This Zeeman contribution has been discussed in details in this thesis.

1.5 Thesis organization

The thesis presents the perpendicular and parallel field magneto-transport studies on epitaxially grown Bi_2Te_3 topological insulator thin films on Si(111). The films have been grown by molecular beam epitaxy and characterized by reflection high energy electron diffraction, scanning tunnelling microscopy, x-ray photoelectron spectroscopy, x-ray diffraction and magneto-transport studies. Chapter 2 gives a short introduction on epitaxial growth methods and different growth modes, the growth system, and different characterization systems. The detailed description of growth and structural characterizations are given in Chapter 3. Chapter 4 discusses about the transport measurements and analysis of the experimental data with various theories. The analysis of the thesis is summarized in Chapter 5.

2

Overview of growth and characterization techniques

2.1 Growth technique

Excellent material quality, homogeneity and uniformity of growth, and precise control over the film thickness are some of the essential criteria required in modern day technology. A film grown on a substrate may be amorphous, polycrystalline or single crystalline. The crystallinity of the grown film depends on the material of the film and the substrate, the substrate temperature and the growth technique. To grow single crystalline film with good quality, epitaxial techniques are suitable among other various methods.

2.1.1 Epitaxial growth

Epitaxy is ordered growth of a crystalline film on a pre-existing single crystalline substrate [67, 68]. The term epitaxy has Greek origin, *epi* meaning above and *taxis* meaning an ordered manner. So epitaxy could be translated as arrange upon. The

film, which is deposited on the substrate, is called the epitaxial film or epitaxial layer or epilayer. In epitaxial growth, the epitaxial film takes the lattice structure identical or similar to the substrate, and the epilayer becomes locked into one or more crystallographic direction of the substrate that acts like a seed layer. Epitaxy of the grown film can be on a substrate of same composition, the process is then termed as homoepitaxy. Otherwise, if the composition of the deposited film and the substrate is different, the process is called heteroepitaxy.

There are various epitaxial growth techniques, the main difference being in the supply of the source material: the film may be grown from gaseous, liquid or solid precursors. In the last few decades, modern techniques like chemical vapor deposition, metal-organic chemical vapor deposition, molecular beam epitaxy (MBE) etc. have been developed. A brief description of the MBE technique, that has been used for this work, is given below.

2.1.2 Molecular Beam Epitaxy

Molecular beam epitaxy is one of the most popular and simplest growth technique, where under ultra high vacuum (UHV) condition extremely-pure source materials are evaporated thermally or by ion-beams and are deposited in a controlled rate onto a substrate maintained at a fixed temperature [69, 70]. The UHV pressure in an idle growth chamber in MBE is in $\sim 1 \times 10^{-10}$ mbar range, and the UHV condition is maintained by combination of pumps such as turbo molecular pump, ion pump and titanium sublimation pump. The UHV condition allows growth of very high quality epitaxial films with a very low deposition rate. The UHV maintains the source fluxes in the molecular flow region, where the mean free path of the molecules is much larger than the system geometry, and the molecules of the source material do not collide or

react before reaching the substrate. The MBE growth chamber is also equipped with a *in-situ* reflection high energy electron diffraction system which helps monitoring the growth process as the epilayer is built up one atomic layer at a time.

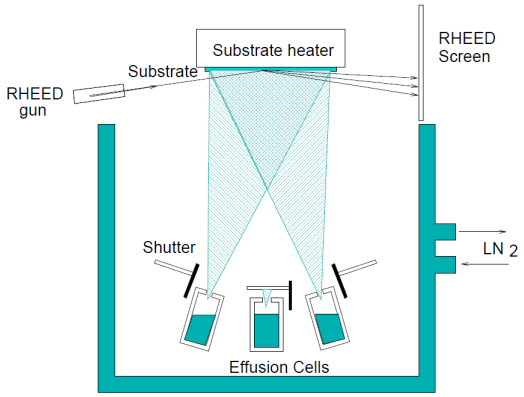

Figure 2.1: Schematic diagram of a typical MBE chamber showing its main components (taken from [68]).

Figure 2.1 is a schematic sketch showing the components of a typical MBE growth chamber. The material source is either a Knudsen type effusion cell (thermal evaporator) or e-beam evaporator. The source material is kept in an inert crucible, and the crucible is heated either by radiation from a heater coil in a Knudsen type cell or by bombarding with an electron beam in an e-beam evaporator. The cell opening (aperture) is covered by a tantalum shutter which can be opened or closed from outside to control the effusion of material from the cell through the aperture. The vapor pressure of the material can be controlled by setting the temperature of the cell for a Knudsen cell or by setting the voltage and current of the e-beam in an e-beam evaporator. To monitor the vapor presser of the molecular beam, an ion-gauge-based beam flux monitor (BFM) is kept in the path of the molecular beam near the substrate but not obstructing the substrate. The growth rate and thickness of the epilayer is determined from a quartz thickness monitor that senses the change in frequency of the quartz crystal when material is deposited on it. The uniformity in thickness and

the composition of the film depend on the uniformity of the molecular fluxes, the ratio of the fluxes for a compound growth, and the distance between the cell and the substrate. The substrate is kept in the center which is at an equal distance from all the cells. In some systems, there is an option for rotation of the substrate with a constant angular velocity around the axis perpendicular to its surface. This rotation enhances uniformity in thickness and homogeneity in composition. There is a heater in the substrate for holding the substrate temperature to a desired value through resistive heating. There is also a direct heating wire connected to the substrate which passes direct current through the substrate.

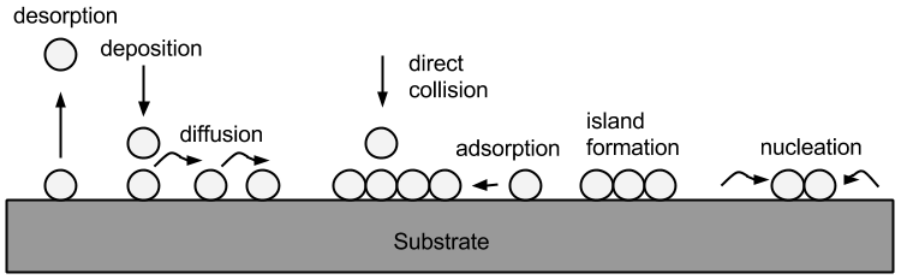

Figure 2.2: Schematic representation of various surface processes associated with growth (adapted from [68, 70]).

The temperature of the substrate is very crucial for the quality of the epitaxial film. During growth the substrate is conventionally kept at moderately high temperature to improve the crystallinity of the epitaxial film. The effect of heating is diffusion of ad-atoms, out diffusion of extra atoms and impurities, and migration of atoms in the lattice sites of the substrate for better arrangement of atoms in the epitaxial film. The temperature should not be so high as to induce diffusion of atoms between the substrate and the grown epilayer. Figure 2.2 shows various surface processes such as re-evaporation or out-diffusion or desorption, adsorption, surface diffusion, nucleation,

clustering or island formation, direct impingement and incorporation of constituent ad-atom etc. that are involved in growth. The effect of heating also may give rise to temperature induced strain in the epitaxial film which determines in turn growth modes and the epitaxial quality of the grown film. Annealing after growth at the growth temperature or at a higher temperature than growth temperature also helps in obtaining a good quality epitaxial film. There are different ways of heating the substrate, either during growth or after growth. Annealing can be done at a higher temperature than growth temperature, or growth can be directly performed at a higher temperature followed by annealing at the growth temperature or an even higher temperature. There is a another two step method in which the growth is started at lower temperature, and, without changing the source flux, the substrate temperature is increased and the growth is completed at elevated temperature along with annealing at that temperature. Depending on the method, the growth of epitaxial film on the substrate can be optimized.

2.1.3 Epitaxial growth modes

The quality of the surface of the substrate has great influence on the initial stage of the growth process of the epitaxial film. The factors that influence the growth are lattice misfit between the grown film and the substrate, thermal stress due to elevated substrate temperature during growth, the chemical interaction between the film and the substrate, any lattice dislocation in the grown film during initial growth stage, etc. Depending on these factors, there are various growth mechanisms by which the epitaxial film grows. The three main growth modes [68, 67, 70] are named after their original investigators: the Frank van-der Merve mode (FM mode) or the layer-by-layer growth mode, the Volmer Webber mode (VW mode) or the island

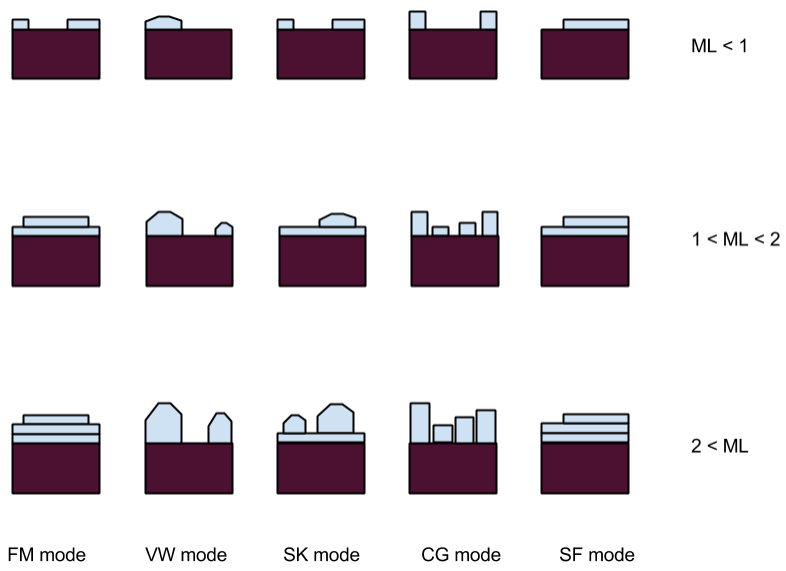

Figure 2.3: Schematic representation of various growth modes in epitaxy for different monolayer (ML) coverage (adapted from [67, 68, 70]).

growth mode, and the Stranski Krastanov mode (SK mode) or the layer plus island growth mode. Besides these three growth modes, there are two more possible mode of epitaxial growth: Columnar Growth (CG) mode and Step Flow (SF) growth mode. Figure 2.3 shows the schematic of various growth modes.

Three important factor determines the quality of the heteroepitaxial layer: lattice misfit between the substrate and the heteroepitaxial layer, crystallographic orientation of the substrate and the surface geometry or surface reconstructions. Lattice mismatch between the substrate and the epitaxial grown film plays an important role in inducing strain in the epilayer. The strain energy serves as a driving force in determining the growth mode. Figure 2.4 shows a strained pseudomorphic growth of the epilayer in the case of lattice mismatch. Strain is also a dominant source of imperfections and dislocations in the epilayer. The growth process in a heteroepitaxy also depends on whether the grown epilayer is coherent or non-coherent with the substrate. In the coherent case, the epitaxial layer adopts the in-plane crystallographic

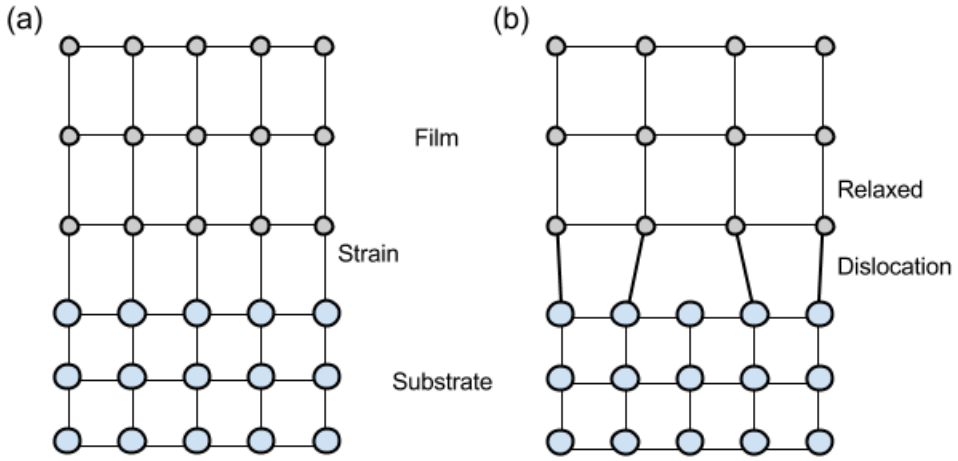

Figure 2.4: Illustraion of strain and relaxed dislocation growth in case of lattice mismatch (adapted from [68, 70]): (a) Lattice mismatch developes strain in the film, but no dislocation of film crystal happens. (b) There is no strain in the film, but dislocation at the interface happens due to lattice mismatch.

direction and the lattice constant of the substrate. In the non-coherent case, the epilayer is free to take any lattice structure and the epilayer adopts that particular in-plane lattice which minimizes its surface energy.

The surface geometry, surface reconstructions and presence or absence of dangling bonds in the surface strongly determine the quality of the heteroepitaxial layer. It is difficult to grow a good epitaxial layer on top of dangling bonds unless there is good lattice matching between the substrate and the epilayer. However lattice misfitted material with no dangling bonds provides an excellent hetero epitaxial film on a clean (reconstructed) surface via van-der Waal's forces. This type of epitaxy is called van-der Waal (vdW) epitaxy. It allows fabricating of very abrupt interfaces with very few defects and a very good quality heterostuctures. This vdW epitaxy is only limited to quasi-one or quasi-two dimensional materials in which atoms of a unit layer are attached to each other by strong covalent bond but layers are held together by weak

vdW forces. So one can easily cleave the two layer without creating any dangling bonds. With the three dimensional structure, one can passivate the dangling bonds on a clean surface that should be stable on relative high growth temperature. Thus, one can create quasi vdW gaps, and vdW epitaxy then can be possible. Figure 2.5 shows the possibility of vdW epitaxy in case of dangling bond, in absence of dangling bonds or in passivated dangling bonds on the sample surface.

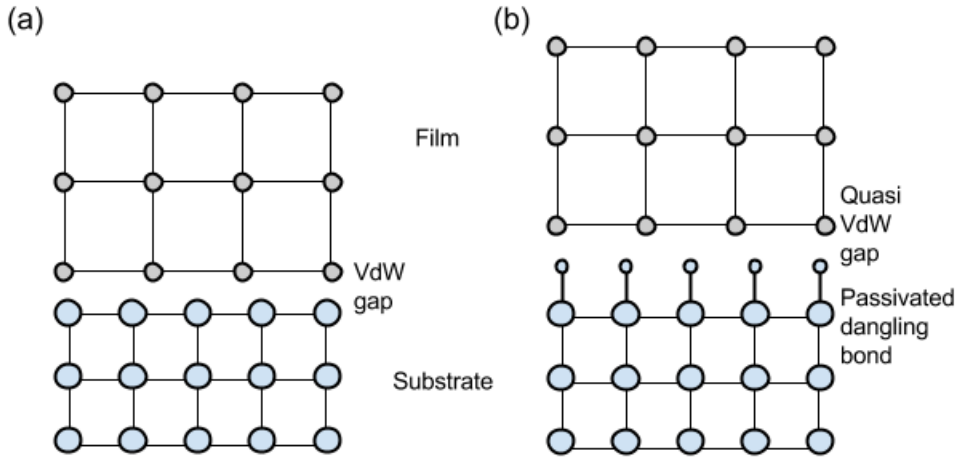

Figure 2.5: Illustration of vdW and quasi vdW epitaxy (adapted from [71]): (a) vdW epitaxy for no dangling bonds in the surface, (b) quasi vdW epitaxy for passivated dangling bonds in the surface.

2.2 Characterization techniques

The morphology of the surface, the sharpness of the interface, the quality of the crystals, the compositions of the material are properties that are important to understand the quality of the epitaxially grown layer. Various structural characterization techniques are used to confirm the material and crystalline quality of the grown film. The film can be further analyzed by measuring its electrical transport properties. The

crystalline quality was investigated *in situ* during growth by reflection high energy electron diffraction (RHEED), and after growth *ex situ* x-ray diffraction (XRD) can be used to confirm the crystalline quality and the thickness of the film. The surface morphology can be analyzed by scanning tunnelling microscopy (STM) and the chemical compositions of the grown material can be verified by x-ray photoemission spectroscopy (XPS). Each of the techniques, which has been used in this work, is discussed in details in the following sections.

2.2.1 Reflection High Energy Electron Diffraction

Reflection High Energy Electron Diffraction is a *in situ* surface sensitive technique that is used to examine qualitatively the properties of the epitaxial thin film during growth. The experimental set up for RHEED consists of an electron gun, a focusing electrical lense and a phosphorus screen. The electron gun and the focusing lense are kept at one end and the screen is kept at the opposite end, both the ends being far apart from the substrate to keep open space for deposition. In a typical RHEED set up, very high energy (10 keV - 100 keV) electrons are emitted from the gun and are incident on the substrate with a grazing angle ($< 3^0$), the diffracted beam produces a pattern on the phosphorus screen. The grazing angle incidence allows the electron beam to penetrate only a few atomic layer near the surface of the sample, which produces surface sensitivity. The higher the energy of the incident electrons is, the sharper the features appears on the screen. Thus RHEED features give information about the sample surface, the crystalline quality of the grown film and the growth modes.

The RHEED diffraction pattern contains information about the unit cell and the

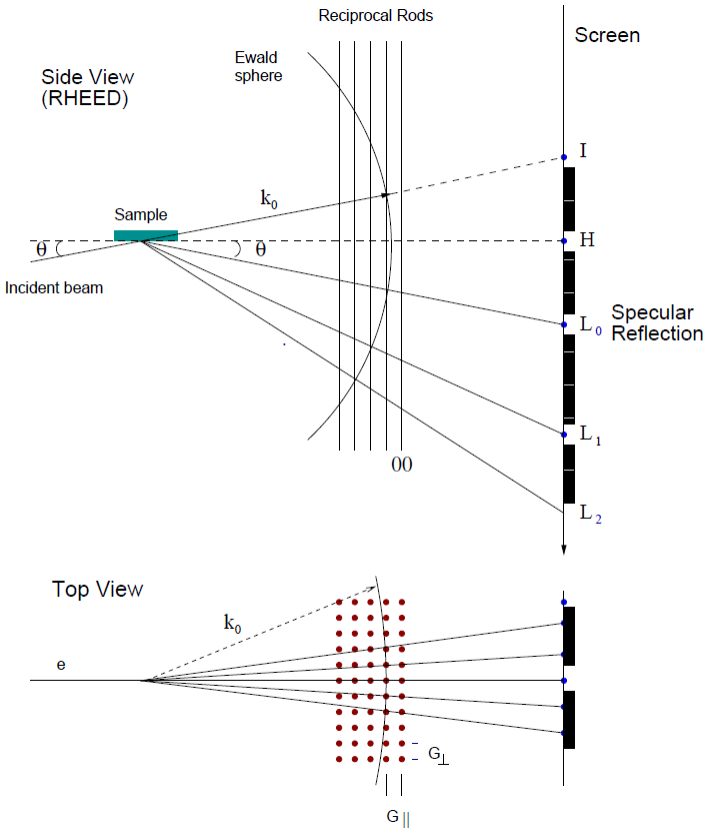

Figure 2.6: Ewald sphere construction and diffraction pattern in RHEED (taken from [68]).

crystal structure. The condition for diffraction satisfy the Laue criteria,

$$\vec{k} - \vec{k}_0 = \vec{G}_{hkl}, \tag{2.1}$$

where $\vec{k}_0$ is the incident wave vector, $\vec{k}$ is the diffracted wave vector and $\vec{G}_{hkl}$ is the reciprocal lattice vector connecting the origin to the reciprocal lattice point (h, k, l). For elastic scattering,

$$\left|\vec{k}\right| = \left|\vec{k}_0\right|. \tag{2.2}$$

The Laue criterion is geometrically visualized by constructing an Ewald sphere, which is a sphere of radius $\left|\vec{k}_0\right|$ centered at the origin of $\vec{k}_0$. So according to the Laue criteria,

diffraction occurs for all $\vec{k}$ connecting a reciprocal lattice point on the sphere to the origin. As RHEED is only surface sensitive, a perfect crystal surface is a 2D lattice plane as seen by the incident electrons. The associated reciprocal lattice consists of 1D rods perpendicular to the surface passing through the lattice points. The diffraction pattern according to the Laue condition by constructing an Ewald sphere, is shown in Figure 2.6. The reciprocal rods are continuous in the direction normal to the surface, so each rod satisfies the Laue condition to produces a diffraction pattern on the screen as shown in Figure 2.6. In Figure 2.6, I is the projection of the origin of the reciprocal lattice, L_n (n = 0, 1, ...) are the radius of different Laue circles centered at H, $G_{\parallel}$ and $G_{\perp}$ are separation of rods in parallel and perpendicular direction with respect to the beam respectively.

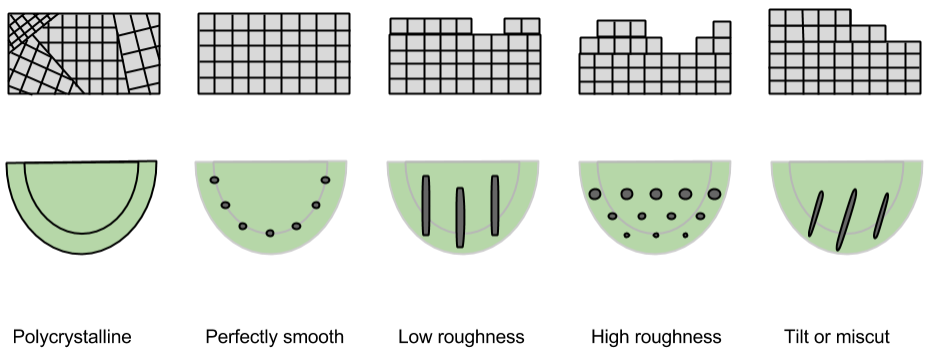

Figure 2.7: Schematic representation of RHEED pattern for different type of surfaces (adapted from [68]).

RHEED patterns give information about the crystalline quality of the sample surface. Figure 2.7 shows different type of RHEED pattern for different surfaces. For a polycrystalline surface the diffraction pattern will be broad rings called the Debye-Scherrer rings. For a perfect flat crystal surface the pattern will be spots along a semicircle. A low roughness (order of one-two monolayer) surface gives sharp streaky patterns. A surface with a very high roughness (island growth) produces 3D net of

spots and a tilted surface gives tilted streak pattern. By monitoring the intensity of the spots on the RHEED pattern during growth, the growth mode can be identified. For the FM (layer by layer) growth mode , the intensity of a spot oscillate in time (as the growth proceeds) with same amplitude. For the VW (island) growth mode, the intensity of a spot sharply decreases with time. For the SK (layer plus island) growth mode, the intensity oscillate in time with a decreasing amplitude of oscillation. In the SF (step flow) mode, the intensity first deceases and then increases, no oscillations are observed as film morphology remains same.

2.2.2 Scanning Tunnelling Microscopy

Scanning tunnelling microscopy has become very popular since the 1986 Nobel Award winning discovery by Gerd Binning and Heinrich Rohrer. STM is capable of imaging conducting surfaces directly in the real space at the atomic scale. A block diagram of STM is shown in Figure 2.8. The main components of an STM consist of an atomically sharp tip, one scan generator, feedback electronics and computer system. Apart from these, two important components are the coarse-approach system and the vibration isolation system.

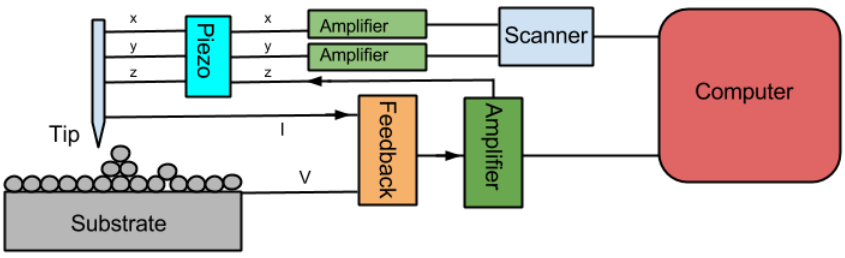

Figure 2.8: Schematic circuit diagram of a typical STM set up (adapted from [68]).

Scanning tunnelling microscopy is based on quantum mechanical tunnelling of

electron from the surface to the STM tip via the intermediate space. The tunnelling probability decreases exponentially as the distance between the surface and the tip increases. STM takes advantage of this extreme sensitivity to distance. The sharp metallic STM tip is positioned within a few angstroms of the conducting surface of the sample. A voltage bias is applied between the tip and the sample surface, near enough that the wave function of the electron in the STM tip and in the surface overlapped and couple. The electrons tunnel from the surface to the tip through the intervening space (the tunnelling barrier) or vice verse depending on the polarity of the applied bias. The tunnelling current depends on the tunnelling probability. As the tip is scanned over the surface, the tunnelling current varies along the surface. There are various modes of operation. In the constant current mode, the STM tip is moved up and down to hold the current constant, following the contours of the surface or, more precisely, the electron local density of states (LDOS) on the surface. In the constant height mode, the current variation is tracked while the height of the STM tip remains fixed. The computer system registers this variation in height or tunnelling current, respectively, and processes this information into a topographic image of the surface. There is also a scanning tunnelling spectroscopy mode where the above is performed as a function of applied bias between the tip and the surface to obtain the LDOS as a function of energy.

2.2.3 X-ray Photoemission Spectroscopy

X-ray photoemission spectroscopy is a quantitative technique that determines chemical compositions of a material and electronic states of constituting elements in the material. XPS is based on the photoelectric effect discovered by Einstein. An usual XPS set up has a source, an electrical lens, a hemispherical analyzer and an electron

detector. The source can be monochromatic Al-Kα or non-monochromatic Mg-Kα. The X-rays emitted from the source are focused on the sample and electrons with various kinetic energies are generated. The generated electrons are either photo-electrons (electrons ejected due to a direct transition) or Auger electrons (electrons ejected due to an indirect transition). These electrons then are focused by the electric lens, and after passing through the hemispherical analyzer the focused electrons are recorded in the detector. A typical XPS spectrum shows the number of electrons detected by the XPS detector versus the binding energy or the kinetic energy of the detected electrons. The kinetic energy of an ejected electron is related to the binding energy of the electron in the material by,

$$E_k = h\nu - E_b + \phi_s, \tag{2.3}$$

where h is the Planck constant, ν is the frequency of the X-ray photons, E_b is the binding energy and ϕ_s is the spectrometer work function. A XPS spectra consists of both the photo-electrons and the Auger electrons. The photo-electrons give sharp peaks, which are the characteristic peaks at a characteristic binding energy that helps to identify the elements present on the surface of the material. The Auger electrons produce a wide peak in the background spectra. These characteristic peaks of photo-electrons correspond to the electronic configuration of the electrons within the atoms. In a compound, the characteristic peak of the constituent element gets shifted from its original position due to oxidation or reduction state of the atom in a chemical bonding. XPS spectra help to determine chemical bonding from such peak shift of individual elements. The chemical compositions also can be found from the ratio of the peak areas.

2.2.4 X-Ray Diffraction

X-Ray diffraction is a very powerful non-destructive technique to study crystal structure. Crystalline quality, crystal structure, atomic arrangement, stress and defects in a crystal are studied using XRD. Film thickness can also be determined from XRD. The XRD set up consists of three main parts: a fixed source, a rotating sample stage and a rotating detector. The source is made up of three primary parts: a cathode ray tube with Cu as the target material, a monochromator which selects Cu-Kα radiation, and a collimator. Inside the cathode ray tube, a filament is heated by passing current, and electrons are ejected from the heated filament. The electrons are then accelerated towards the target Cu by applying a voltage. The high energy electrons then hit the Cu material and characteristic Cu-K alpha radiation is emitted. The wavelength of the Cu-K alpha radiation is 0.154 nm. The monochromator selects a narrow wavelength band around that wavelength of x-ray radiation, and the x-rays are collimated and directed onto the sample. The detector records the x-ray photon count after the radiation passes through an attenuator attached in front of the detector. The detector can rotate along the incident beam direction (characterized by a rotation angle 2θ, where 2θ is the angle between incident beam and the diffracted beam). The direct beam axis is the axis joining source to the detector at the $\theta = 0^0$ position. The sample stage is also movable. The sample stage can move sideways (in a predefined local x-y coordinate frame), can rotate around the axis z perpendicular to the stage (ψ rotation, where ψ is the angle between direct incident beam axis and the local x axis of the stage), can rotate around the direct incident beam axis (ϕ rotation, where ϕ is the angle measured in perpendicular direction to θ), and can rotate in the incident beam direction (ω rotation, where ω is the angle of incidence). The different angles of rotation and axis are shown in Figure 2.9.

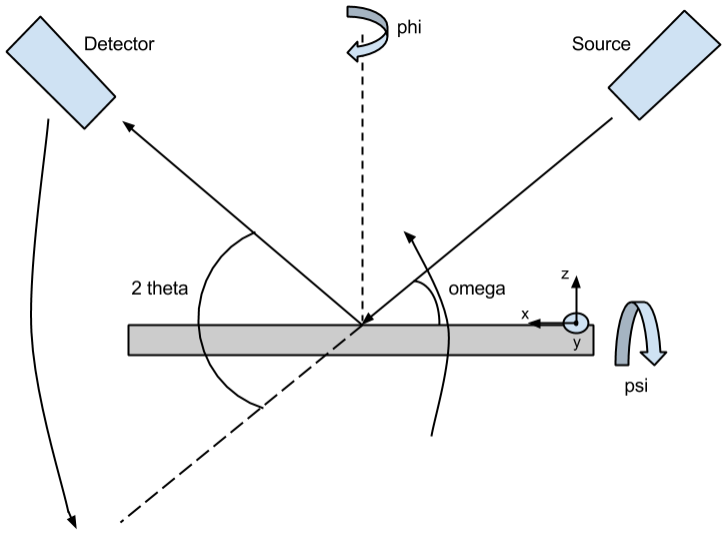

Figure 2.9: Schematic representation of a typical XRD set up showing various angles and axis.

The incident X-rays are diffracted from the sample and the diffracted rays form constructive or destructive interference pattern. In a typical $2\theta - \omega$ XRD scan, the stage rotates by an angle ω and the detector rotates an angle 2θ. The X-ray intensity will vary with the position of the stage and the detector, tracking this interference pattern. The XRD spectra consists of peaks in the recorded intensity at certain 2θ angles due to constructive interference of diffracted beams at that position. The condition for constructive interference is given by the Bragg's Law,

$$2dsin\theta_B = n\lambda. \tag{2.4}$$

Here, $\theta_B$is called the Bragg angle, n is the order of diffraction, λ is the wavelength of the X-ray radiation, and d is the distance between two lattice planes. If the Miller indices of the lattice plane is given by (h, k, l), then distance between two such plane is $d_{hkl} = 2\pi/G_{hkl}$, where G_{hkl} is the length of the reciprocal lattice vector from the

origin to the (h, k, l) point in the reciprocal space. From the positions of the peak, the crystal structure can be calculated using Equation 2.4. The peak width and relative intensities are also important to determine the crystal structure and the quality of the crystal. The peak intensity varies depending on the structure factor, and some peaks are not present due to a zero structure factor. The effect of strain and thermal expansion, grain size, and coexistence of different phases can be determined from the peak position and broadening. The thickness of the film can also be calculated from the relative positions of two fringes. The formula to calculate thickness is,

$$t = \frac{n_1 - n_2}{2(sin\theta_1 - sin\theta_2)}, \tag{2.5}$$

where t is the measured thickness, n_1, n_2 are order of the fringes from the main peak $(n = 0)$ and θ_1, θ_2 are corresponding fringe position in the XRD spectra.

2.2.5 Physical Property Measurement System

The Quantum Design physical property measurement system has two options: DC and/or AC transport measurement capable of measuring electrical and thermal conductivity, and magnetic measurements using a vibrating sample magnetometer. The system is capable of doing measurements up to 9T magnetic fields and cooling samples down to 2 K. The magneto-transport experiments in this work were conducted using standard van-der Paw geometry in a DC set up.

3

Growth and characterization of Bi_2Te_3 thin film on Si(111)

The Bi_2Te_3 thin film was grown in a custom-built MBE growth chamber equipped with *in-situ* RHEED. The MBE growth chamber is connected to a UHV (pressure $\sim 1\times10^{-10}$ mbar) surface analysis chamber that is equipped with variable temperature STM, XPS and other surface analysis techniques. The *in-situ* surface analysis have been done in the UHV surface analysis chamber and the XRD has been done *ex-situ*. These results have been published in [72].[1]

[1]Part of Chapter 3 (section 3.3, 3.4 and 3.5) has been published in Applied Physics Letters 102, 163118 (2013) (reference [72] in this thesis) *titled* Two-dimensional weak anti-localization in Bi_2Te_3 thin film grown on Si(111)-(7×7) surface by molecular beam epitaxy *by* Anupam Roy, Samaresh Guchhait, Sushant Sonde, Rik Dey, Tanmoy Pramanik, Amritesh Rai, Hema C. P. Movva, Luigi Colombo and Sanjay K. Banerjee. The contribution of the authors to this paper is as follow: Sanjay K. Banerjee has conceived, designed and supervised the experiments. Anupam Roy has grown the sample in MBE and has done the XPS and STM characterizations, with assistance from me, Sushant Shonde, Tanmoy Pramanik and Amritesh Rai. Luigi Colombo has helped us with his insightful comments and suggestions on the growth and characterization part. Samaresh Guchhait has done the XRD and transport measurements with help from me, Tanmoy Pramanik and Hema C. P. Movva. I and Tanmoy Pramanik have done the transport data analysis. Anupam Roy and I have written the paper. All authors have discussed and commented on the final manuscript.

3.1 MBE cell calibration

In the MBE growth chamber, the molecular beams of the constituent elements (Bi and Te) were thermally generated from Knudsen type effusion cells. The vapor of the element is generated inside the cell and effuses through the cell aperture to create the molecular flux. The non-ideality of the cell and other cell parameter result in dependence of the flux to the cell geometry and amount of element present in the cell. Thus it is important to calibrate the flux of the constituent element.

The vapor pressure P_c of a material inside the cell is related to the cell temperature T_c by [73],

$$P_c = Ae^{-B/T_c}, \tag{3.1}$$

where A and B are material dependent constant. The flux density of the molecular beam effusing from the cell can be calculated using theory of ideal gas and is given by [73],

$$j = \frac{a}{\pi r^2} cos\theta \frac{P_c}{\sqrt{2\pi m k_B T_c}},$$

where a is the area of cell aperture, r is the distance between cell aperture and substrate, θ is the angle at which the cell aperture is oriented with respect to the substrate, m is the mass of the molecule and k_B is the Boltzmann constant. So equivalently it can be written as,

$$j = A' e^{-B/T_c} / \sqrt{T_c}, \tag{3.2}$$

where A' depends on the particular material, cell and chamber geometry.

The growth rate is proportional to the molecular flux effused from the cell aperture. One way of calibration is to get the growth rate from the quartz thickness monitor. The thickness is determined from the change in frequency of the quartz crystal due

to the added mass. The actual thickness is calculated from the recorded one using the following formula,

$$\text{Actual thickness} = \text{Displayed thickness} \times \frac{\text{Density given to monitor}}{\text{Actual Density of material deposited}} \times \frac{100}{\text{Tooling factor in \%}}. \tag{3.3}$$

For better precision in display monitor, lowest value possible for density is given to the thickness monitor control. The tooling factor can be calculated from system geometry. In this case the tooling factor is taken to be 100% because of nearly same distance of the thickness monitor and the substrate from the cells.

The other way to calibrate the cell is by using beam flux monitor (BFM) to get the beam equivalent pressure (BEP). BEP is the reading of the beam flux monitor exposed to a molecular beam minus the base pressure of the chamber, i.e.,

$$\text{BEP} = \text{BFM pressure - Base pressure.} \tag{3.4}$$

The flux monitor is calibrated for N_2 gas in room temperature T_R. One needs to convert the recorded BEP correctly to an actual vapor pressure. The BEP of a material is given by [73],

$$\text{BEP} = I\frac{T_R}{T_c}\frac{a}{4\pi r^2}P_c,$$

where I is the ionization cross section. So one can write

$$\text{BEP} = A''e^{-B/T_c}/T_c, \tag{3.5}$$

where A'' is another parameter which depends on the particular material, cell and

chamber geometry.

It is interesting to note that the temperature dependent part of vapor pressure differs from flux by a factor of $\sqrt{T_c}$ (Equation 3.1 and Equation 3.2) and the temperature dependent part of flux differs from BEP by a factor of $\sqrt{T_c}$ (Equation 3.2 and Equation 3.5). However, the exponential dependence on temperature is same for vapor pressure, flux and BEP. So for a given material, in a log-linear plot with respect to inverse temperature, all of them give straight lines parallel to each other for small range of temperatures [73]. Also the plot between flux and BEP is linear in the temperature range of interest and the proportionality factor (depends on system geometry) needs to be calibrated once for a given material.

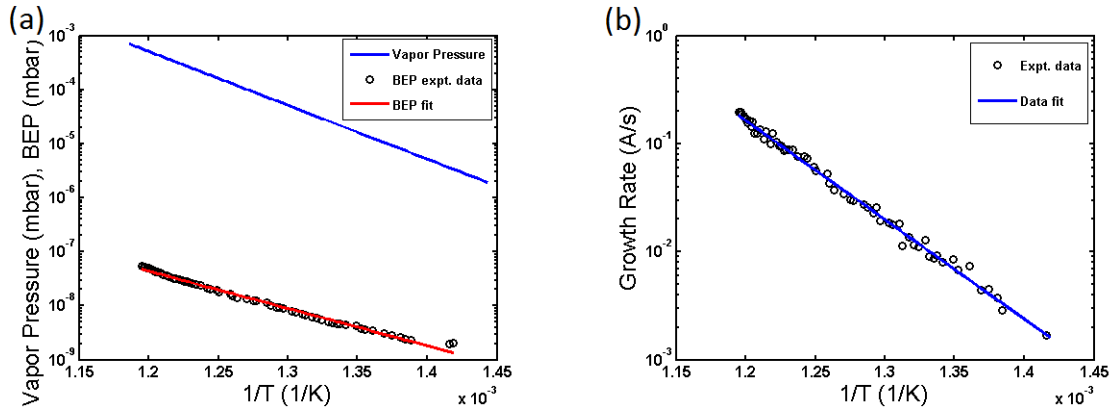

Figure 3.1: Calibration of Bi: (a) Experimental data and theoretical fitting of Vapor pressure and BEP for Bi. (b) Experimental data and theoretical fitting of growth rate for Bi.

Bi powder of high quality (99.99 %) was thermally evaporated from the effusion cells. Figure 3.1 shows the calibration data for BEP and growth rate of Bi for temperature range of $450K - 560K$. Variation of vapor pressure and BEP of Bi are plotted against inverse of the cell temperature in a log-linear plot and shown in Figure 3.1(a), where the green line is the original vapor pressure and the red line is the fit to the

data points for BEP. The original vapor pressure of Bi obeys:

$$P_{Bi}\ (\text{in mbar}) = e^{19.93-2.29\times10^4/T}. \tag{3.6}$$

The formula after fitting the BEP data is obtained to be:

$$\text{BEP}_{Bi}\ (\text{in mbar}) = e^{2.099-1.59\times10^4/T}. \tag{3.7}$$

The growth rate is similarly plotted in in Figure 3.1(b) with inverse of temperature in a log-linear plot and the straight line is the fit to the data. The growth rate (GR) can be fitted by:

$$\text{GR}_{Bi}\ (\text{in angstrom/s}) = e^{23.58-2.11\times10^4/T}. \tag{3.8}$$

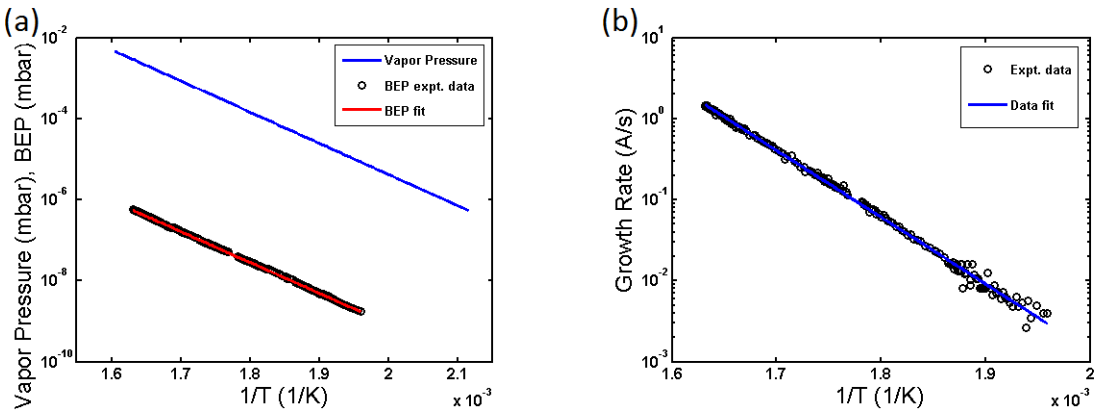

Figure 3.2: Calibration of Te: (a) Experimental data and theoretical fitting of Vapor pressure and BEP for Te. (b) Experimental data and theoretical fitting of growth rate for Te.

Te was also evaporated from effusion cell filled with Te powder of high quality (99.99 %). Figure 3.2 shows the calibration data for BEP and growth rate of Te for temperature range of $240K - 340K$. Variation of vapor pressure and BEP of Te are plotted against inverse of the cell temperature in a log-linear plot and shown in

Figure 3.2(a), where the green line is the original vapor pressure and the red line is the fit to the data points for BEP. Similarly the growth rate is also plotted in Figure 3.2(b) and a fit is obtained. The formula for vapor pressure of Te is:

$$P_{Te} \text{ (in mbar)} = e^{23.058 - 1.771 \times 10^4 / T}. \tag{3.9}$$

The fitting for BEP of Te is obtained as:

$$\text{BEP}_{Te} \text{ (in mbar)} = e^{14.22 - 1.755 \times 10^4 / T}. \tag{3.10}$$

Similarly the growth is fitted and the temperature variation is given by:

$$\text{GR}_{Bi} \text{ (in angstrom/s)} = e^{31.37 - 1.90 \times 10^4 / T}. \tag{3.11}$$

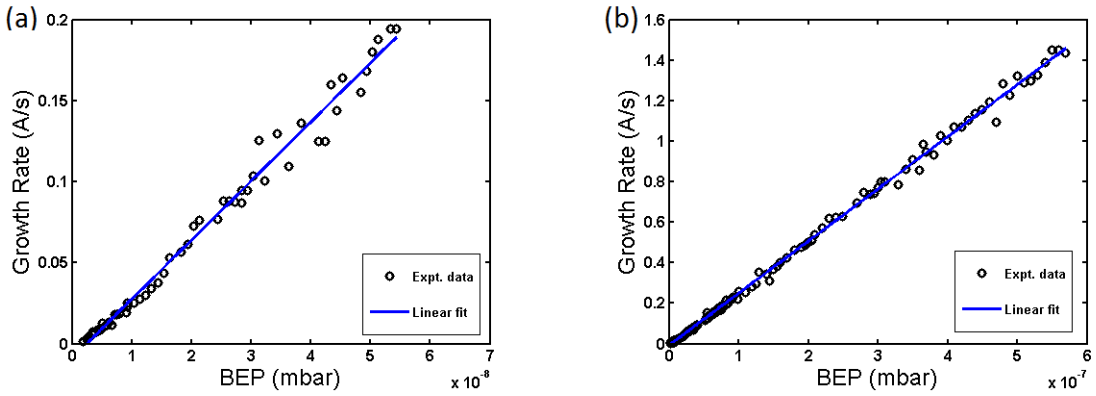

Figure 3.3: Calibration of growth versus BEP: (a) Experimental data and theoretical fitting of growth vs BEP for BI. (b) Experimental data and theoretical fitting of growth rate vs BEP for Te.

There is a linear relationship between the growth rate and BEP for a given material. Figure 3.3 shows the relationship between growth rate and BEP for Bi and Te. The data are also fitted to a straight line. The fitting to data for Bi in Figure 3.3(a)

produces

$$\mathrm{GR}_{Bi}\ (\text{in angstrom/s}) = 3.646 \times 10^6 \times \mathrm{BEP}_{Bi}\ (\text{in mbar}). \tag{3.12}$$

Similarly growth rate for Te, shown in Figure 3.3(b), obeys:

$$\mathrm{GR}_{Te}\ (\text{in angstrom/s}) = 2.574 \times 10^6 \times \mathrm{BEP}_{Te}\ (\text{in mbar}). \tag{3.13}$$

3.2 Substrate selection

In literature, Bi_2Te_3 has been studied in either bulk crystal form, or exfoliated flake from bulk crystal or has been grown in MBE on different substrate such as GaAs(001)[32], GaAs(111)[33], sapphire(0001)[34], $SrTiO_3$[35], Si(111)[36, 37, 38, 24] and so on. The quality of the grown film depends much on the film-substrate combination due to lattice mismatching. The lattice mismatch is calculated for different surface of Si and for different growth direction of Bi_2Te_3, the lowest lattice mismatch occurs for two cases. For Si(001) substrate, if the $[1\bar{1}00]$ direction of Bi_2Te_3 is parallel to the $[1\bar{1}0]$ direction of the substrate, the lattice mismatch will be 14%. For Si(111) substrate, if the $[11\bar{2}0]$ direction of Bi_2Te_3 is along the $[11\bar{2}]$ direction of the substrate, the lattice mismatch will be 14%. Here Si(111) is a choosen over Si(001) surface for growing Bi_2Te_3. Since there are van-der Waal forces between different QLs of Bi_2Te_3, the growth process occurs in van-der Waal epitaxy mode, and comparatively large lattice mismatch between Bi_2Te_3 and Si(111) surface can be relaxed. The growth of Bi_2Te_3 on Si is important as it will offer a way of integrating TI with Si technology for future device application.

3.3 Substrate preparation

The high quality Bi_2Te_3 film was grown on Si(111) surface by MBE. The substrate was cut from P-doped n-type Si(111) wafer (oriented within $\pm 0.5^o$) with resistivity 1-20 Ω - cm. The sample was cleaned with Methanol, Acetone and Isopropyl alcohol before loading into the high vaccum MBE chamber. The substrate was first degassed in resistive heating followed by direct heating at about 600^0 C for 12-14 hours and then flashed at about 1200^0 C for 1 minute [72]. The sample was then cooled down to room temperature and the atomically clean surface is observed by *in-situ* RHEED. Figure 3.4 shows the (7 $\times$ 7) surface reconstruction of the Si(111) surface. Figure 3.4(a) shows the reconstruction from $[11\bar{2}]$ incidence direction and Figure 3.4(b) is from $[1\bar{1}0]$ incidence direction.

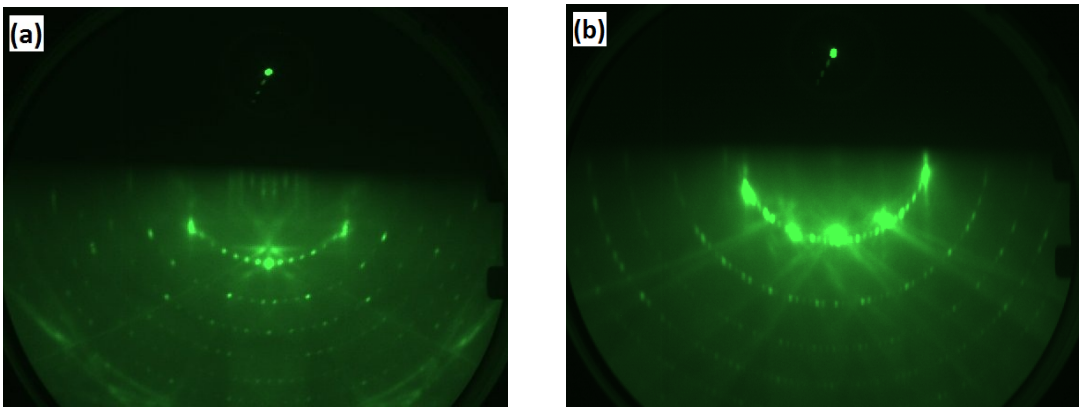

Figure 3.4: The RHEED pattern for (7 $\times$ 7) surface reconstruction for atomically clean Si(111) surface (published in [72]): (a) from $[11\bar{2}]$ incidence direction. (b) from $[1\bar{1}0]$ incidence direction.

3.4 Bi_2Te_3 growth and *in-situ* characterization

Krumrain et. al.[38] have optimized the growth of Bi_2Te_3 thin film by MBE and studied the effect of substrate temperature, cell temperature and flux ratio to the

growth morphology. The best flux ratio of Te to Bi is about 20 and the optimum substrate temperature is 350^o C to 450^o C. Also Te atmosphere is needed after the growth until the substrate temperature falls below 350^o C to compensate Te out-diffusion. In this case, the Te and Bi cell temperatures were maintained such that $T_{Te} > T_{sub} > T_{Bi}$ and the beam equivalent pressure ratio was $BEP_{Te}/BEP_{Bi} \sim 20$ [72].The base pressure of the chamber was $\sim 1 \times 10^{-10}$ mbar and the pressure during growth never exceeded 5×10^{-8} mbar. Te and Bi flux were generated from effusion cell calibrated before and the fluxes were co-deposited onto Si(111)-(7×7) substrate with substrate temperature of 350^o C. The cell temperature for Bi was 540^0C and cell temperature of Te was 320^0C. The growth is done for 5 minutes with a rate of 0.8 nm/min. After the growth the sample is annealed for 10 minutes with the same substrate temperature in a Te overpressure environment.

3.4.1 RHEED

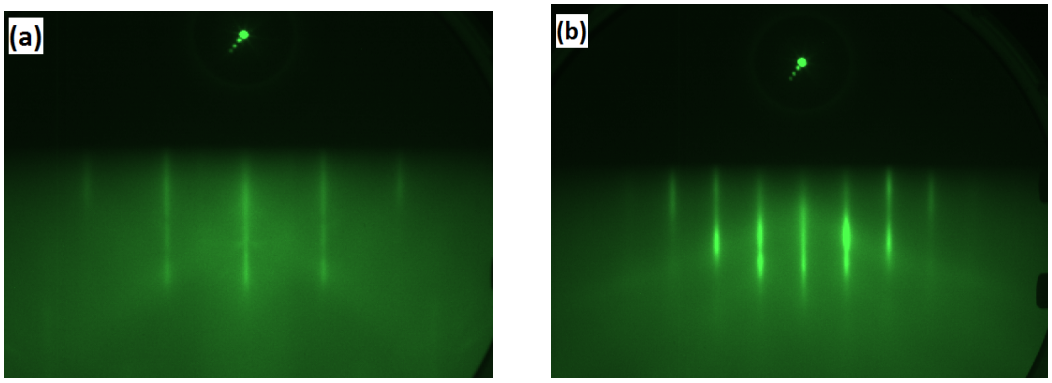

Figure 3.5: The RHEED pattern of the same surface after growth of Bi_2Te_3: (a) from $[11\bar{2}]$ incidence direction of Si substrate. (b) from $[1\bar{1}0]$ incidence direction of Si substrate.

Figure 3.5 shows the RHEED images of the epitaxially grown Bi_2Te_3 thin film just after the growth. The image in Figure 3.5(a) is taken from the $[11\bar{2}]_{Si}$ incidence

direction of the Si(111) substrate and Figure 3.5(b) is taken from the $[1\bar{1}0]_{Si}$ incidence direction of the Si(111) substrate. The RHEED image shows sharp streaky lines indicating an atomically sharp morphology and coincident latticed matched growth of Bi_2Te_3 on Si(111) surface despite lattice mismatching between them. Figure 3.6 shows the RHEED images of the grown Bi_2Te_3 thin film just after the 10 minutes annealing. The image in Figure 3.6(a) and Figure 3.6(b) are taken from the $[11\bar{2}]_{Si}$ and the $[1\bar{1}0]_{Si}$ incidence direction of the Si(111) substrate, respectively. After annealing there is no significant change but the streaky pattern becomes sharper.

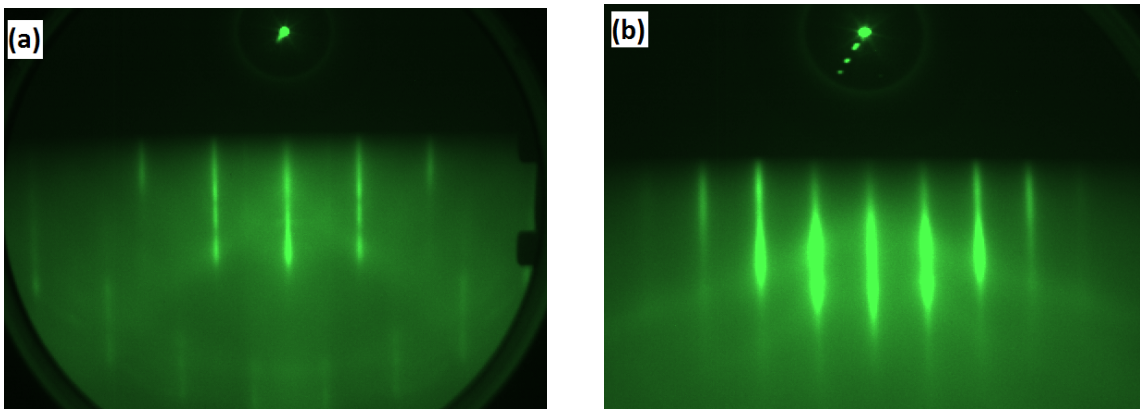

Figure 3.6: The RHEED pattern of the same surface after 10 minutes annealing of grown Bi_2Te_3 (published in [72]): (a) from $[11\bar{2}]$ incidence direction of Si substrate. (b) from $[1\bar{1}0]$ incidence direction of Si substrate.

3.4.2 STM

Figure 3.7(a) shows the STM image of Bi_2Te_3 surface with a step. The height profile of the step is shown in Figure 3.7(b). The step height is $\sim$ 1 nm and indicates height of one QL. The expected growth direction is along [001] i.e. the c-axis of the Bi_2Te_3 crystal structure.

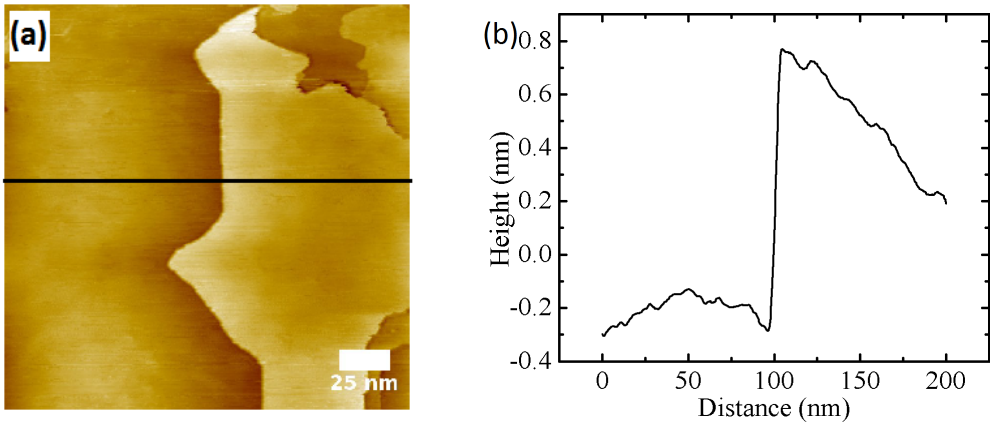

Figure 3.7: The STM image of Bi_2Te_3 surface (published in [72]): (a) 200 nm × 200 nm tomographic image. (b) Height profile along the line shown in (a).

3.4.3 XPS

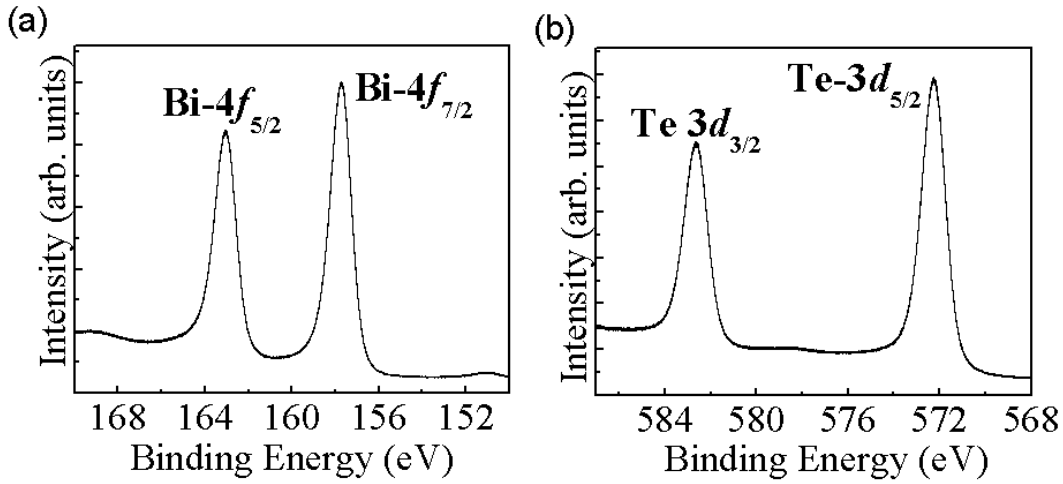

Figure 3.8: The XPS spectra of Bi_2Te_3 surface (published in [72]): (a) Bi-4f peak positions, (b) Te-3d peak positions.

The chemical composition of the grown film was analyzed by *in-situ* XPS study. Figure 3.8 shows the XPS peak for each individual component- Bi and Te. The peaks for Bi is shown in Figure 3.8(a), two peaks corresponds to Bi-$4f_{7/2}$ and Bi-$4f_{5/2}$ splitting with binding energies 157.7 eV and 163.1 eV respectively. Similarly the peaks for Te is shown in Figure 3.8(b) with Te-$3d_{5/2}$ and Te-$3d_{3/2}$ splitting at energies

572.3 eV and 582.6 eV respectively. The splitting is due to the corresponding outer shell electronic configuration of Bi and Te. The peaks show a shift with respect to those from a pure bulk material. The Bi-4f has a blue shift while the Te-3d is red shifted. The shifts in Bi and Te are in opposite direction which indicates Bi-Te chemical bonding and charge transfer from Bi to Te.

3.5 Bi_2Te_3 *ex-situ* characterization

The crystallinity, growth direction and thickness of the MBE grown Bi_2Te_3 thin film on Si(111) sample were obtained from the corresponding XRD curve.

3.5.1 XRD

Figure 3.9 shows the rocking curve for the Si(111)/Bi_2Te_3 sample measured in $2\theta - \omega$ arrangement. The XRD data shows that the crystalline quality of the grown film is very good. The XRD spectra consists of peaks from the Si substrate, the sample stage (Al) and the Bi_2Te_3 thin film. The peaks for Bi_2Te_3 belongs to the $h = 0 = k$ and $l = 3n$ family, where only [0006], [00015] and [00018] peaks are visible. The XRD data shows that the crystalline quality of the grown film is very good. Despite having a lattice mismatch of 14% of Bi_2Te_3 with the substrate, the grown film is crystalline. The good crystallinity of the film may be due to coincidence lattice match or good lattice match between the supercells of Bi_2Te_3 and Si(111) substrate. A Bi_2Te_3 supercell of 1 interatomic distance along the $[21\bar{3}0]$ direction and 3 interatomic distance along the $[01\bar{1}0]$ direction matches closely with a supercell of Si(111) consisting of 2 interatomic distance along the $[1\bar{1}0]$ direction and 2 interatomic distance along the $[11\bar{2}]$ direction [36]. The lattice mismatch between Si and Bi_2Te_3 are 1.1% along the $[11\bar{2}]$ and 0.9% along the $[1\bar{1}0]$ directions of Si [36]. Such small mismatch may be

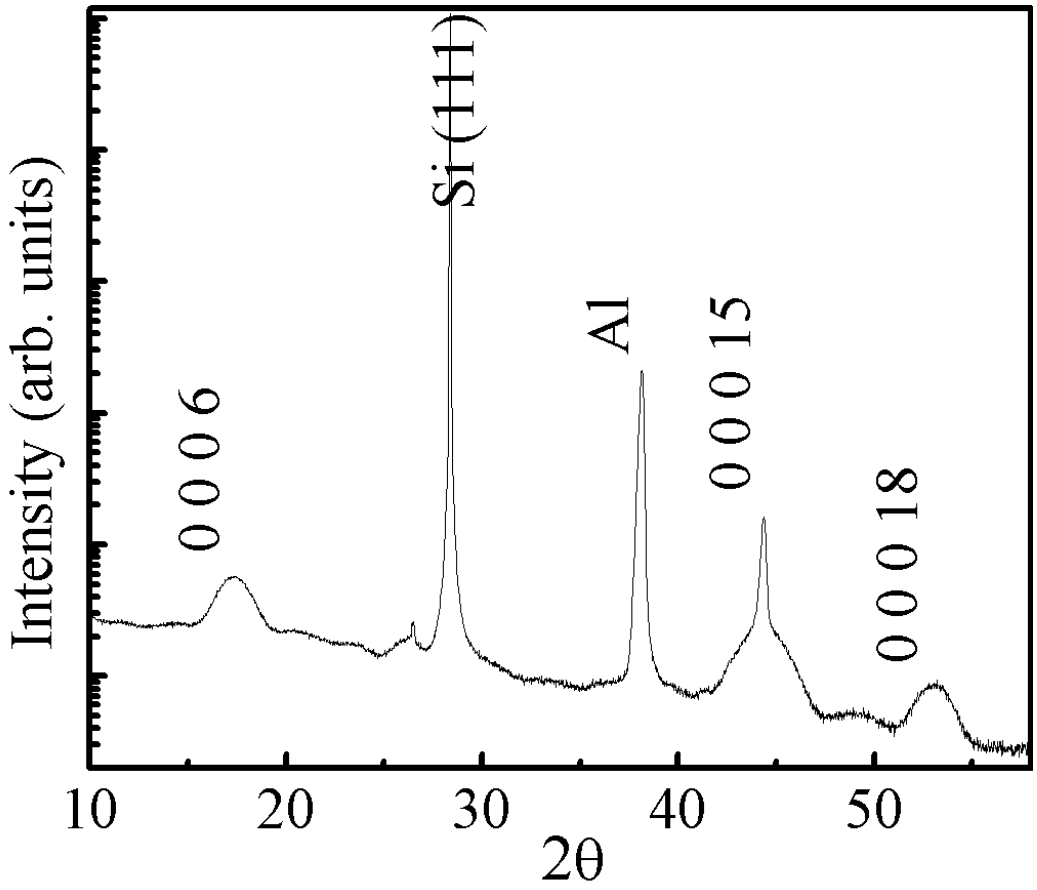

Figure 3.9: The XRD spectra of Bi_2Te_3/Si(111) sample showing peaks for substrate Si, Bi_2Te_3 thin film and the sample stage (aluminium) (published in [72]). The $h = 0 = k$ and $l = 3n$ family of peaks are present for Bi_2Te_3, and the side fringes for the [0006] peak gives an estimate for thickness.

responsible for such good crystal quality of the film. The film thickness is also evaluated from the XRD data using the peak positions of the [0006] peak of the thin film and its nearest fringe. The thickness comes out to be about 4 nm.

4

Transport study on Bi_2Te_3 thin film

The magneto-transport studies are done on the sample using the standard Van der Pauw geometry and standard DC measurement in a physical property measurement system, with magnetic fields up to 9 T and temperature down to 2 K. All the resistance data are collected by averaging over 100 measurements. The magnetoresistance data have been taken for both positive and negative magnetic fields to eliminate parasitic voltage effects. These results have been published in [72, 74].[1]

[1]Chapter 4 has been published partly in Applied Physics Letters 102, 163118 (2012) (reference [72] in this thesis) and partly in Applied Physics Letters 104, 223111 (2014) (reference [74] in this thesis). The contribution to Applied Physics Letters 102, 163118 (2012) paper has been mentioned before in the footnote of Chapter 3. The contribution of the authors, to the Applied Physics Letters 104, 223111 (2014) paper *titled* Strong spin-orbit coupling and Zeeman spin splitting in angle dependent magnetoresistance of Bi_2Te_3 *by* Rik Dey, Tanmoy Pramanik, Anupam Roy, Amritesh Rai, Samaresh Guchhait, Sushant Sonde, Hema C. P. Movva, Luigi Colombo, Leonard F. Register and Sanjay K. Banerjee, is as follow: Sanjay K Banerjee has conceived, designed and supervised the experiments. I have done the transport data measurements with help from Tanmoy Pramanik, Samaresh Guchhait and Hema C. P. Movva. I have analysed the data with help from Tanmoy Pramanik. Anupam Roy has grown the sample in MBE and has done the XPS and STM characterizations, with assistance from me, Sushant Shonde, Tanmoy Pramanik and Amritesh Rai. Luigi Colombo has helped us with his insightful comments and suggestions on the growth and characterization part. I have written the paper. Leonard F. Register has helped me in analyzing the data and writing the paper. All other co-authors have discussed and commented on the final manuscript.

4.1 Resistance vs Temperature

The longitudinal resistance is plotted with temperature from 2 K to 300 K, which is shown in Figure 4.1. Around 180 K, the resistance starts to increase as carriers in the bulk Si substrate starts to freeze out. The carriers in the Si substrate completely freeze out at around 130 K. Below 130 K, only the carriers in the Bi_2Te_3 film contributes to the resistance and the resistance shows a metallic drop up to 20 K. Below 20 K, the resistance increases as the temperature decreases, which corresponds to an insulating behavior. The film has an insulating ground state which arises from the electron-electron interaction and has been discussed further in coming sections. The longitudinal resistance versus temperature is measured again with an magnetic field of 5 T applied perpendicular to the surface. With an applied magnetic field, the resistance have the same trend up to 20 K, but below 20 K the two resistance differs as shown in the inset of Figure 4.1. This difference is due to suppression of localization in an applied magnetic field, which has been discussed too in the coming sections.

4.2 Perpendicular Field Magnetoresistance

The transverse resistance or the Hall resistance and the longitudinal resistance or the magnetoresistance (MR) are measured at very low temperature with a perpendicularly applied magnetic field, and are shown in Figure 4.2. The Hall resistance, with the magnetic field B perpendicular to the sample surface at 2 K, is shown in Figure 4.2(a). The Hall resistance is linear with field, which is clear from the linear fitting shown in Figure 4.2(a). From the slope of the Hall resistance, we determined the charge carriers to be electrons with a sheet carrier density of 1.2×10^{14} cm^{-2}. The MR at 2 K, with a magnetic field perpendicular to the sample surface, is shown in Figure 4.2(b). The

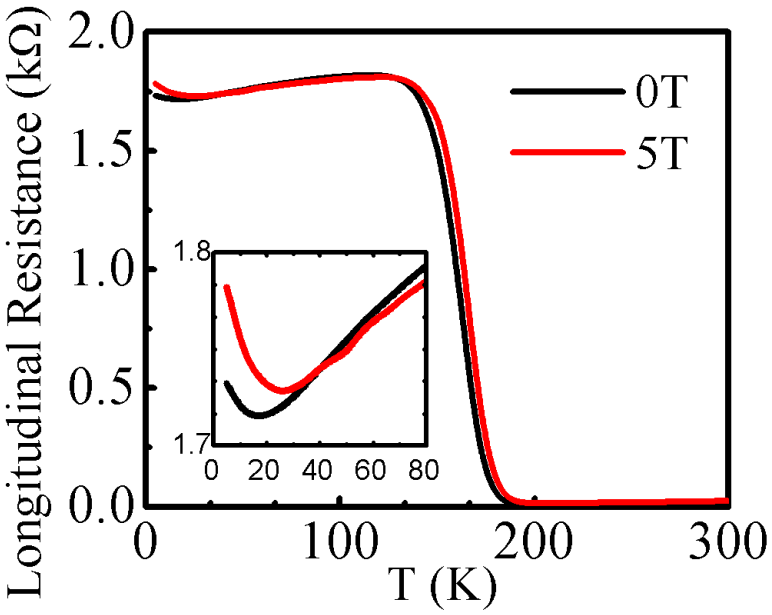

Figure 4.1: Temperature dependence of longitudinal resistance for temperature varying 300 K to 2K (published in [72]).

perpendicular field MR has a sharp dip at small fields and the MR is linear for high fields. The dip corresponds to the suppression of WAL effect in a magnetic field and can be explained with the simplified HLN equation [64, 72]:

$$\begin{aligned}\Delta\sigma(B) &= \frac{\alpha e^2}{2\pi^2\hbar}\left[\psi\left(\frac{1}{2}+\frac{B_\phi}{B}\right)-\ln\left(\frac{B_\phi}{B}\right)\right] \\ &= \frac{\alpha e^2}{2\pi^2\hbar}\eta\left(\frac{B_\phi}{B}\right)\end{aligned} \tag{4.1}$$

where, $\Delta\sigma(B) = (\sigma(B) - \sigma(0))$ is the change of magnetoconductivity, e is the electronic charge, $\hbar$ is the reduced Planck constant, $B_\phi = \hbar/(4el_\phi^2)$ where l_ϕ is the phase coherence length, $\psi(x)$ is the digamma function $d\Gamma(x)/dx$, and $\eta(x)$ is defined as $\eta(x) = (\psi(x+\frac{1}{2}) - \ln(x))$. α is a fitting parameter with a theoretical value of 1, 0 and -0.5 for orthogonal, unitary and simpletic case respectively [64]. Therefore α should be -0.5 for WAL in a single surface in a TI and -1 for both the surface channels.

The MR is fitted with $R(B) \approx R(0) - \Delta\sigma(B)R^2(0)$ using Equation 4.1 for small fields (0-1 T), as shown in Figure 4.2(b). We obtained a fitting parameter of $\alpha = -0.54$ denoting presence of a single channel.

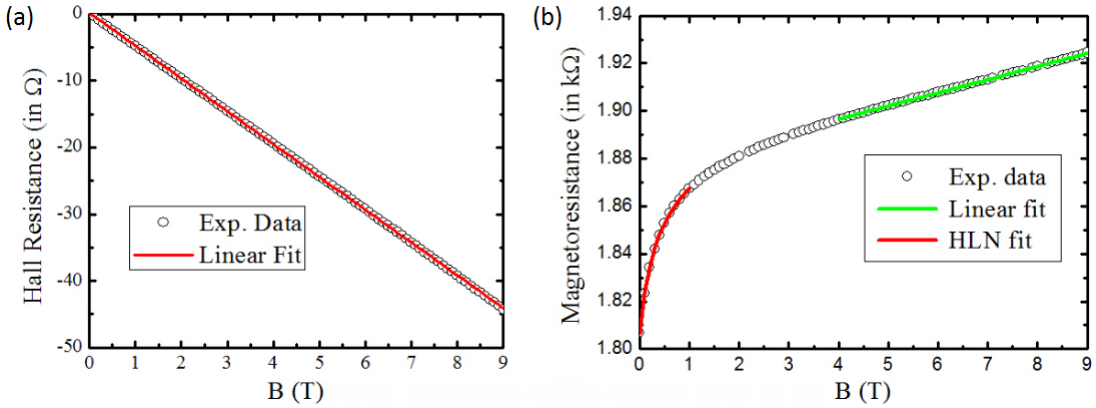

Figure 4.2: Hall resistance and MR with a magnetic field applied perpendicular to the surface at 2 K (published in [72]): (a) Hall resistance shows linear dependence with field. (b) MR is fitted with HLN for small field and MR shows linear behavior for large fields.

The linear Hall resistance for higher magnetic fields and an α value near -0.5 for WAL effect in the MR suggests the presence of only one strongly coupled system of carriers with a single type of carrier. However, the high carrier density implies presence of electrons in the bulk CB along with in the surface states. Also, the electronic transport in this film behaves as a 2D electron gas, that has been obtained from further experiment and argument given in coming sections. This is possible, because in the thin film limit due to confinement in one direction, the otherwise 3D bulk states are subdivided into parallel 2D sub bands [26, 27, 55]. The top, bottom and surface states become strongly overlapped and, therefore, strongly coupled through scattering, which allow the system behaving like a single phase-coherent 2D channel [26, 27, 49, 72, 75].

We have estimated the Fermi energy from the electron concentration obtained from

the slope of the Hall resistance. We have assumed a parabolic dispersion relation for the nominally bulk CB subbands with effective mass $m^* \approx 0.178 m_e$ [76], where m_e is the free space rest mass of an electron. We have also taken the bottom of bulk CB being about 0.3 eV above the nominal Dirac point [13]. Although, as a gap Δ opens up in the nominally surface states, near the Fermi energy ($\varepsilon_F \gg \Delta$) the dispersion relation is linear with $v_F \approx 4.0 \times 10^5$ m/s [13, 42]. The estimated Fermi energy ε_F = 0.58 eV. The Fermi wave vector $k_F \approx \varepsilon_F / \hbar v_F$ is estimated to be 2.2 nm^{-1}, similar value has been reported in literature [42]. However, these estimates of ε_F and k_F are approximate, as a gap Δ opens up in the nominally surface states making the dispersion relation parabolic, and nominally CB sub-band states are only roughly characterizeable by an effective mass approximation.

4.2.1 Weak Antilocalization Effect

The low field dip in the perpendicular field MR is due to the suppression of WAL effect in an applied magnetic field. We have further investigated the MR behavior for different temperatures ranging from 2 K to 20 K. Figure 4.3(a) shows the perpendicular field MR for entire 0-9 T field range for different temperatures, where the dots represent the experimental data. We first tried to fit these data using Equation 4.1 for the 0-1 T field range for different temperatures, as shown in the same figure, where the solid lines show the fit. As we increase the temperature, the dip in MR broadens and finally disappears because with increasing temperature the phase coherence length decreases. The phase coherence length $l_\phi = (D\tau_\phi)^{1/2}$, where D is the diffusion constant and τ_ϕ is the phase coherence time. With increasing temperature the phase coherence time decreases so the phase coherence length decreases. The phase coherence length l_ϕ is obtained from the fitting parameter B_ϕ and is plotted with

temperature, T, in Figure 4.3(b). The variation of l_ϕ with temperature T is fitted by $l_\phi \propto T^{-\frac{1}{2}}$. So $\tau_\phi \sim T^{-1}$ indicates 2D nature of carrier. Also $\tau_\phi \sim T^{-1}$ indicates that the decoherence mechanism is due to electron-electron interaction [77] and not due to electron-phonon interaction, as electron-phonon interaction would provide $\tau_\phi \sim T^{-3}$ [78].

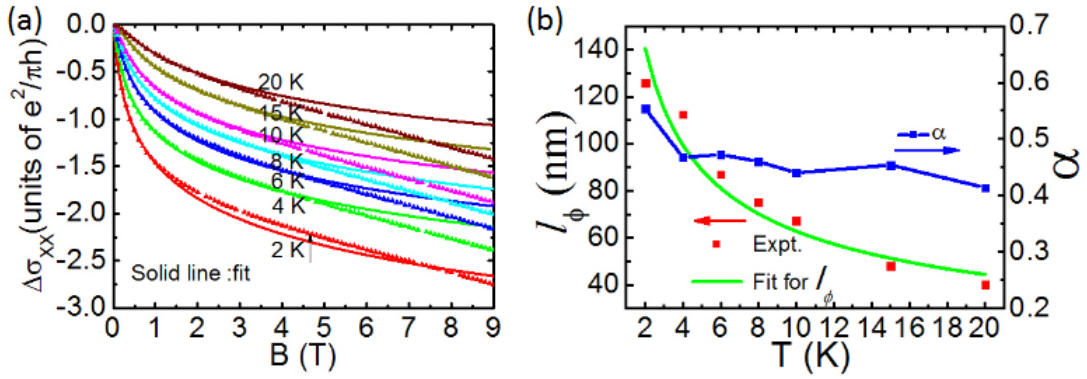

Figure 4.3: Weak Antilocalization at small fields (published in [74]): (a) Data fitting in 0 - 1 T field range using simplified HLN formula, data shows WAL effect, (b) variation of phase coherence length and with temperature, extracted by curve fitting in (a).

We have fitted the perpendicular field MR in 0 - 1 T field range using the simplified HLN equation which is valid only in low field and strong SOC regime. The fitting is done for data points in the 0 - 1 T field range and the fitted curve is plotted for the entire range upto 9 T. It is clear that the fitted curve matches with the experimental data for small fields, but the deviation of experimental values from the fitting curve is significant for large fields. So the simplified HLN equation is insufficient to explain the MR behavior for entire range with the small range fitting parameters. Next we have used the same Equation, i.e. Equation 4.1, to extract the fitting parameters from the entire data range and the fitted curves are shown in Figure 4.4(a). Figure 4.4(a) clearly shows that the fit deviates from the experimental values for both small and large fields. This deviation implies that the full range MR can not be explained by

the simplified version of the HLN equation.

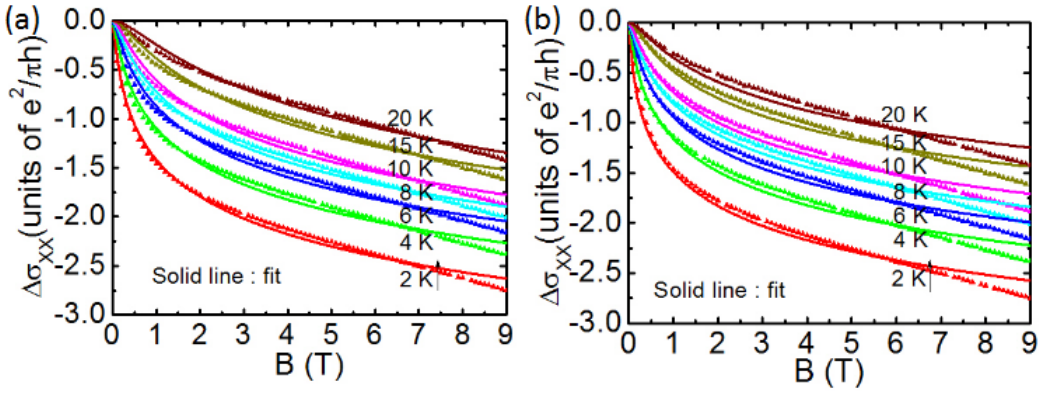

Figure 4.4: Absence of Weak Localization: (a) simplified HLN fitting for data considering entire field range, fitting is not satisfactory. (b) WL fitting for data considering entire field range, fitting is not good either.

The perpendicular MR at large fields is almost linear with fields, as shown in Figure 4.2(b). In literature [79, 80], such large filed linear dependence has been explained using Abrikosov's theory [81] where the required value of magnetic field B, needed for observation of such linear dependence of MR with field arising from electrons in a Dirac cone, is $B = (k_B T + \varepsilon_F)^2/2e\hbar v_F^2$ (where k_B is Boltzmann constant). In our case, the Fermi energy ε_F lies way above the Dirac point and the required value of magnetic field (at $T = 2$ K) is $B \sim 10^3$T $\gg$ 9T, the highest applied magnetic field. There are also a few reports in the literature [26, 28, 75, 82, 83, 84] where such linear MR has been attributed to WL effect in TI films arising from the bulk. To examine whether the transition to the linear dependence of the MR on the magnetic field strength for higher fields is associated with WL effect, we fit our data with [82],

$$\Delta\sigma(B) = \frac{e^2}{2\pi^2\hbar}\left[\frac{3}{2}\eta\left(\frac{\frac{4}{3}B_{SO} + B_\phi}{B}\right) - \frac{1}{2}\eta\left(\frac{B_\phi}{B}\right)\right] \tag{4.2}$$

that addresses both WL and WAL. Here, $B_{SO} = \hbar/(4De\tau_{SO})$ where τ_{SO} is the spin orbit scattering time. In Figure 4.4(b), the fit to MR data using Equation 4.2 is shown,

which is quite reasonable for low fields but not for high fields. The obtained values of B_ϕ are similar to those obtained from fitting Equation 4.1 in the low field region, and the derived B_{SO} that is much greater than B_ϕ, which makes the contribution of the first term in Equation 4.2 negligible for small B (The function $\eta(x)$ approaches zero for large x). The main characteristic of WL is negative MR behavior, which is absent in the data. So the possibility of any WL contribution from the bulk has been excluded even though ε_F is deep inside the CB. Such absence of WL has been seen in the 2D limit of TIs where $\varepsilon_F \gg \Delta$ [19, 75], as topologically-protected states also can arise from topologically non-trivial 2D films with strong SOC, similar to the case of HgTe quantum wells [24, 85, 86].

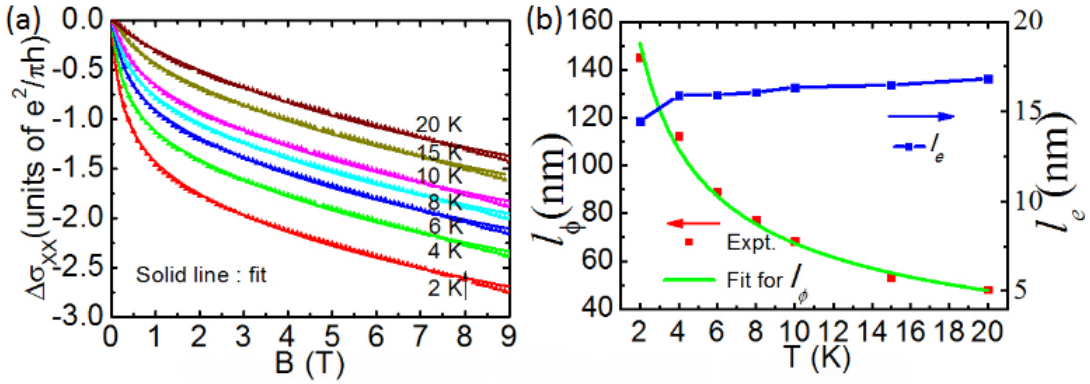

Figure 4.5: Original HLN equation fitting for entire field range (published in [74]): (a) Full range data fitting using original HLN equation. (b) The variations of phase coherence length and mean free path with temperature, extracted from data fit in (a).

We guessed from the fitting using Equation 4.1 and Equation 4.2 that the original HLN equation may describe both the low-field and high-field behaviors. The original

HLN equation [64], which in the case of no magnetic impurity scattering is [87, 64, 74],

$$\Delta\sigma(B) = -\frac{e^2}{2\pi^2\hbar}\left[\eta\left(\frac{B_e}{B}\right) - \eta\left(\frac{B_\phi + 2B_{SO_z} + 2B_{SO_x}}{B}\right) + \frac{1}{2}\eta\left(\frac{B_\phi}{B}\right) - \frac{1}{2}\eta\left(\frac{B_\phi + 4B_{SO_x}}{B}\right)\right] \tag{4.3}$$

Here $B_n = \hbar/(4De\tau_n)$, τ_n is the characteristic time associated with elastic scattering ($n = e$), spin-orbit scattering in x (or y) direction ($n = SO_x$) and spin-orbit scattering in z direction, ($n = SO_z$). Here, the x and y are in the plane of the TI, and z is normal to the plane of the TI. With the condition B, $B_\phi \ll B_e$, B_{SO_x}, B_{SO_z}, i.e. for small fields and large SOC, Equation 4.1 is just the simplified version of Equation 4.3 [64]. These conditions are not true for the entire field range, which is why Equation 4.1 can not properly explain the experimental data, as shown in Figure 4.3(a) and Figure 4.4(a). Equation 4.3 has been used to fit the experimental data, which is shown in Figure 4.5(a). Figure 4.5(a) shows that the fitted curve has an excellent match with the experimental data for both low and high field regions. The condition needed for HLN Equation to be valid in 2D is $d < (\hbar/(4eB)^2)$, where d is the film thickness. In our case $d = 4$ nm and $\hbar/(4eB)^2 = 4.3$ nm for $B = 9$ T. So the HLN Equation is less valid for high fields near 9 T, which is why there are little deviation in fitting near 9 T. The parameter l_ϕ is extracted from the fitting parameters B_ϕ and plotted versus T in Figure 4.5(b). We obtain $l_\phi \propto T^{-\frac{1}{2}}$, similar to that obtained from small range fitting of MR using Equation 4.1 and shown in Figure 4.3(b). The extracted value of $l_\phi = 145$ nm at 2 K is consistent with previous reports [48, 49, 50, 51, 72]. Using $D = (1/2)v_F^2\tau_e$, the elastic scattering length $l_e = v_F\tau_e$ is extracted from the parameters B_e and plotted versus T in the same Figure 4.5(b). Therefore at 2 K, $l_e = 20$ nm and the estimated $k_F l_e$ is ~ 45, similar to that reported before [42, 49, 51], which indicates that the transport is diffusive and ensures the validity

of HLN equation ($k_F l_e \gg 1$). We observed that, at 2 K, the extracted value of B_e is 0.786 T and that of B_{SO_x} is 0.092 T, which are much less than 9 T, the highest field value. This observation explains that Equation 4.1 is not valid to describe the perpendicular field MR over the entire field range, although it can explain the MR data well for small fields (<1 T), because the term in Equation 4.3 corresponding to Equation 4.1 dominates with $B_\phi \ll B_e$, B_{SO_x} and B_{SO_z}. We also have obtained a very large value for the fitting parameter B_{SO_z} satisfying $B_{SO_z} \gg B_e$ for all temperatures, which implies a very small spin-orbit relaxation time (τ_{SO_z}) for the surface-normal direction. This result indicates the presence of strong SOC in this TI, which is consistent with other reports for TIs [87, 88]. In TIs the SOC is so strong that the precession of spin is fast enough to make the out-of plane spin-orbit relaxation time shorter than the elastic scattering time (i.e., $\tau_{SO_z} \ll \tau_e$). However, the in-plane spin-orbit relaxation time is of the same order as the elastic scattering time (i.e., $\tau_{SO_x} \sim \tau_e$) [89] and our obtained value of B_{SO_x} and B_e are comparable. We also noticed that the value of B_{SO_x} is much smaller than B_{SO_z}, i.e. τ_{SO_x} is much larger than τ_{SO_z}, which suggests again that the system is 2D [64]. We have obtained $\tau_{SO_z} \sim 0.2$ fs in the order of $\hbar/\varepsilon_F$ [89]. From fitting we have obtained an upper limit on τ_{SO_Z}, as lowering τ_{SO_Z} below the obtained maximum limit is insensitive to fitting because of the nature $\eta(x)$ function. The actual value of τ_{SO_Z} may be lower than what we have estimated. We have also estimated $\tau_{SO_x} \sim 0.2$ ps and $\tau_e \sim 0.02$ ps at 2 K.

4.2.2 Suppression of Zeeman Effect

The contribution of Zeeman energy in localization and electron-electron interaction have not considered in fitting the MR data with the HLN equation. However, it is clear that the HLN model for WAL alone can describe the perpendicular field MR

behavior in our TI. Now we will discuss whether there are any Zeeman contribution in perpendicular field MR.

Zeeman Effect in Localization

The Zeeman spin splitting energy, which is responsible for mixing spin singlet and triplet states, is not considered in deriving the original HLN equation [64, 65]. Maekawa and Fukuyama have considered the effect of Zeeman spin splitting in their theory of localization for non-interacting electrons [65]. The MR for perpendicular magnetic field considering the Zeeman energy is given by [65, 90],

$$\begin{aligned}\Delta\sigma(B) = -\frac{e^2}{2\pi^2\hbar}\Bigg[\eta\left(\frac{B_e}{B}\right) - \eta\left(\frac{B_\phi + 2B_{SO_z} + 2B_{SO_x}}{B}\right) \\ -\frac{1}{2\sqrt{1-\gamma}}\Bigg[\psi\left(\frac{B_\phi + 2B_{SO_x}\left(1+\sqrt{1-\gamma}\right)}{B}\right) \\ -\psi\left(\frac{B_\phi + 2B_{SO_x}\left(1-\sqrt{1-\gamma}\right)}{B}\right)\Bigg] + \frac{1}{2}\ln\left(1+\frac{4B_{SO_x}}{B_\phi}\right)\Bigg].\end{aligned} \tag{4.4}$$

The ratio $\gamma = (g\mu_B B\tau_{SO_z}/2\hbar)^2$ [49, 90] (g is the Zeeman g-factor and μ_B is the Bohr magneton) determines the correction to the conductivity from the HLN model. Figure 4.6(a) shows our fitting of Equation 4.4 to the MR data over the full field range, which is almost the same as obtained by using Equation 4.3. The values of fitting parameters B_ϕ, B_e, B_{SO_x} are the same, and we obtained a similarly high B_{SO_z} with very small γ. This result is a consequence of strong SOC, as strong SOC implies large B_{SO_z} (small τ_{SO_z}) which makes γ small for our fields of interest. Hence the Zeeman effect in localization is suppressed in perpendicular field MR [49].

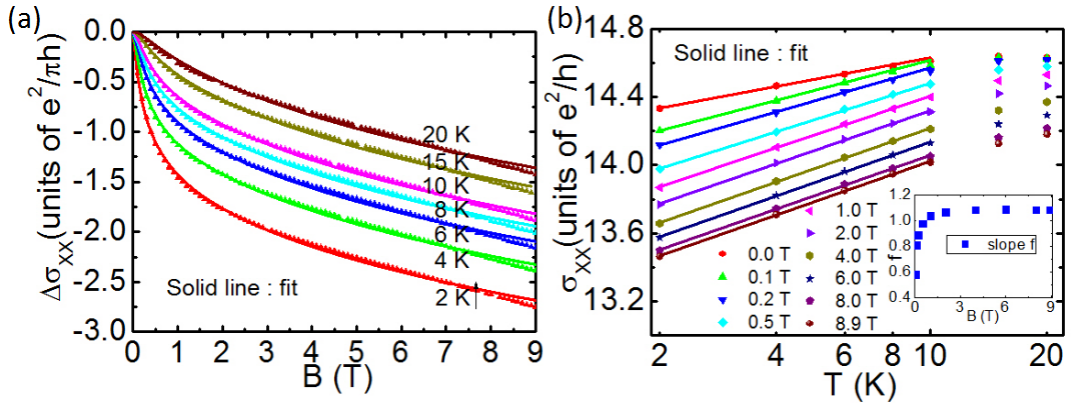

Figure 4.6: Suppression of Zeeman effect in perpendicular field MR: (a) Full range data fit by Maekawa and Fukuyama localization theory in perpendicular field, data fitting is same as that by original HLN equation. (b) The logarithmic dependence of conductivity with temperature, the obtained slope f is plotted with field in the inset of (b) (published in [72]).

Zeeman Effect in Electron-Electron Interaction

Now, we will discuss about the contribution of the Zeeman effect in the EEI theory of Lee-Ramakrishnan [66], where the correction to the Drude conductivity due to temperature and field is given by,

$$\delta\sigma_I(B,T) = \delta\sigma_I'(T) + \delta\sigma_I''(B,T)$$

where,

$$\delta\sigma_I'(T) = \frac{e^2}{4\pi^2\hbar}\left(2 - \frac{1}{2}F_\sigma\right)\ln\left(\frac{T}{T_I}\right) \tag{4.5}$$

$$\delta\sigma_I''(0,T) = -\frac{e^2}{4\pi^2\hbar}F_\sigma\ln\left(\frac{T}{T_I}\right) \tag{4.6}$$

$$\delta\sigma_I''(B,T) - \delta\sigma_I''(0,T) = -\frac{e^2}{4\pi^2\hbar}F_\sigma g_2(B,T) \tag{4.7}$$

Here F_σ, indicating the strength of the Coulomb screening parameter, has a theoretical value between 0 to 1 and T_I is the characteristic temperature for EEI. The asymptotic

formula for the function g_2 is

$$g_2(B,T) = \begin{cases} \ln(\frac{g\mu_B B}{1.3k_B T}), & \text{for } g\mu_B B \gg k_B T \\ 0.084(\frac{g\mu_B B}{1.3k_B T})^2, & \text{for } g\mu_B B \ll k_B T \end{cases} \tag{4.8}$$

Therefore, from Equation 4.7, the field-dependent correction due to EEI for a given temperature and non-zero field is

$$\Delta\sigma_{EEI}(B,T) = (\delta\sigma_I(B,T) - \delta\sigma_I(0,T)) = -(e^2/4\pi^2\hbar)F_\sigma g_2(B,T). \tag{4.9}$$

Figure 4.5(a) shows that the original HLN equation alone can explain the perpendicular field MR and we do not need the $\Delta\sigma_{EEI}(B)$ term from EEI. This result indicates that the Zeeman spin splitting term in EEI (Equation 4.7) is suppressed, which is consistent with previous theoretical and experimental reports [49, 66, 91]. A fitting using EEI theory for perpendicular field MR has been reported before [51], where they have found a small value of F_σ, which also indicates that the effect of EEI is limited. This behavior is again associated with strong SOC. Spin-orbit scattering causes the mixing of up and down spin channels and thus suppresses the spin triplet term contributing to EEI [66]. To observe the effect of spin splitting term in MR, the condition $g\mu_B B \gg \hbar/\tau_{SO_z}$ must be satisfied [66, 92]. Due to small τ_{SO_z} we do not get any contribution from that term in the considered B field range. Although while deriving the EEI theory strong SOC have not been taken into account, no further theory is needed to fit the perpendicular field MR data as HLN theory alone is sufficient to explain it.

However, the singlet term in the EEI theory (Equation 4.5 and Equation 4.6)

should produce a $\ln(T)$ correction with slope [66],

$$f = (2\pi^2\hbar/e^2)[d\sigma/d(\ln T)] = (1 - 3F_\sigma/4). \tag{4.10}$$

The logarithmic dependence of conductivity with temperature is plotted in Figure 4.6(b) where we observe an insulating ground state in our sample which is due to EEI effect as WAL predicts a metallic ground state. For the $\ln(T)$ dependence of magnetoconductivity at zero field, both EEI (the singlet term) and WAL effect are responsible, but the coefficient in the $\ln(T)$ dependence has opposite signs for the EEI and WAL. The effect from localization is [64, 66],

$$\Delta\sigma_L(B = 0, T) = \frac{e^2}{2\pi^2\hbar}\alpha p \ \ln\left(\frac{T}{T_L}\right) \tag{4.11}$$

where $\alpha = 0.5$, $p = -1$ (from the relation $\tau_\phi \propto T^p$), and T_L is a characteristic temperature associated with localization. For higher fields where the WAL effect is suppressed, we should obtain slope of $f = (1 - 3F_\sigma/4)$ from the EEI theory of Lee-Ramakrishnan below the characteristic temperature ($T_L \approx T_I$), which appears to be $\sim$ 20 K in our case. However, the obtained slope f (= 1.05) is about 1 within experimental error. In strong SOC material, the theory of Coulomb interactions in the spin singlet channel explains this difference in slope, as described in literature [57, 93]. Similar experimental results have been reported by others [49, 53, 54]. The corresponding slope f is plotted against field in the inset of Figure 4.6(b). The original HLN equation alone can describe the change of slope f with magnetic field as observed in the experimental data. Therefore, the term $\Delta\sigma_{EEI}(B)$ has no contribution to the perpendicular MR.

We also observed the angular dependence of MR to obtain a better understanding

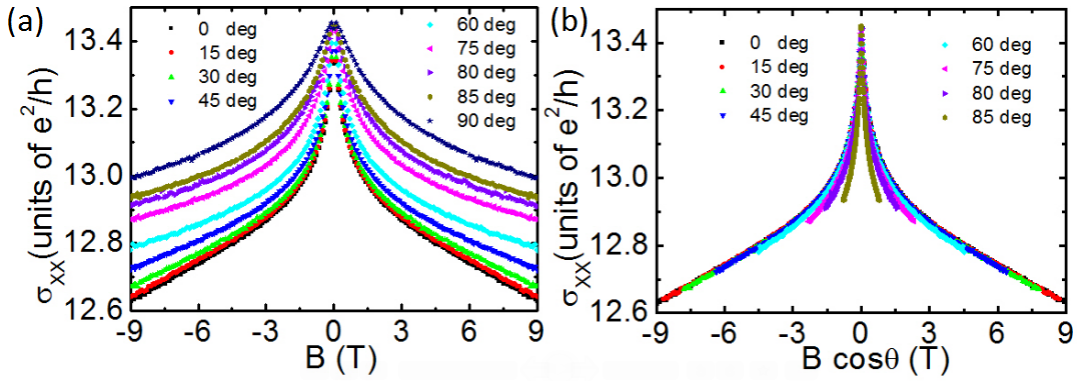

Figure 4.7: Effect of Zeeman splitting in angle dependent MR (published in [72]): (a) The variation of magnetoconductivity with field for different field orientations. (b) The same data as in (a) are plotted with perpendicular component of the field.

of the Zeeman contribution in different field orientations. The magnetoconductivity is shown in Figure 4.7(a) for different field orientations ranging from 0 degrees (for perpendicular field) to 90 degrees (for parallel field). In Figure 4.7(b), the magnetoconductivity for different orientations has been also plotted against the perpendicular component of field. The magnetoconductivity for angles below 45 degrees shows almost no deviation from the no-tilt limit. The magnetoconductivity for tilt angle 60 degrees shows a small deviation. For tilt angles greater than 75 degrees, the deviation is significant and is clearly visible in the magnetoconductivity. This behavior is because the ratio γ is small for small tilt due to large τ_{SO_z}, but γ increases as the tilt increases and becomes nearly 4 times larger at a 75 degrees tilt angle with respect to zero degrees tilt angle. Our result is consistent with other reports [49, 94].

4.3 Parallel Field Magnetoresistance

We have seen that strong SOC suppresses the Zeeman effect and the EEI effect in perpendicular field MR, and only HLN theory of localization is enough to explain the perpendicular field MR data. However, HLN theory of localization has no contri-

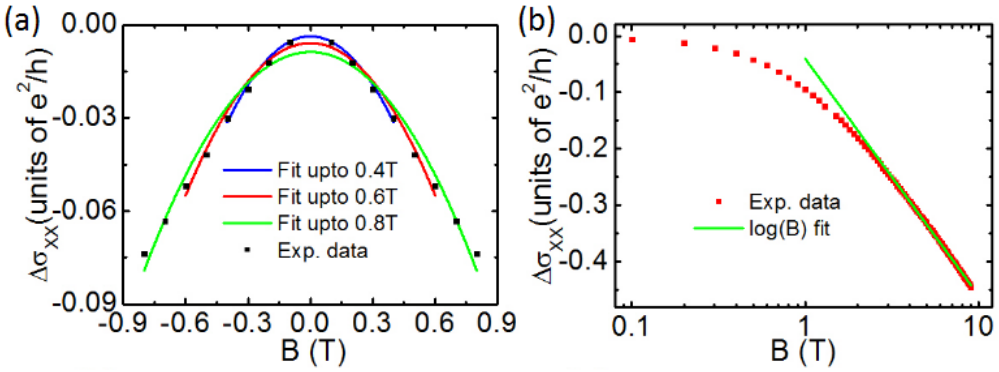

Figure 4.8: MR with field parallel to the surface (published in [72]): (a) B^2 dependence of MR with field for small fields. (b) ln(B) dependence of MR with field at large fields.

bution to MR with magnetic field parallel to the sample surface, and so there must be contributions from the Zeeman effect and the EEI effect. Both the Zeeman effect and the EEI effect produce a parallel field MR that has parabolic dependence with field for low fields and has logarithmic dependence with field for high fields. In Figure 4.8(a), the $\Delta\sigma(B)$ for small field values up to 0.8 T with field parallel to the sample surface has been shown. We fit the data to B^2 dependence for MR at low field for different ranges, but it is clear that the parabolic fit is not good for field ranges greater than 0.4 T. We also have fitted $\Delta\sigma(B)$ data in the large field range with a $\ln(B)$ behavior, as shown in Figure 4.8(b), and from Equation 4.9 the slope $F_\sigma = (4\pi^2\hbar/e^2)[|d\sigma/d(\ln B)|]$ is ~ 0.7.

4.3.1 Localization Effect for non-interacting electrons

The Zeeman effect has been considered by Maekawa and Fukuyama [65] in deriving theory of localization for non-interacting electrons. According to Maekawa and Fukuyama theory of localization, the correction to MR for parallel field is given by

[65, 72],

$$\Delta\sigma_L(B) = -\frac{e^2}{4\pi^2\hbar}\left[\ln\left|1+2\left(\frac{y+z}{x-y}\right)\frac{\tau_\phi}{\tau_e}\right| - \frac{1}{\sqrt{1-\gamma}}\ln\left|\frac{\frac{\tau_e}{\tau_\phi}+\frac{y+z}{x-y}(1+\sqrt{1-\gamma})}{\frac{\tau_e}{\tau_\phi}+\frac{y+z}{x-y}(1-\sqrt{1-\gamma})}\right|\right] \tag{4.12}$$

where $x = \tau_0^{-1}$, $y = \tau_{SO_z}^{-1}$, $z = \tau_{SO_x}^{-1}$ and $\gamma = \left(\frac{g\mu_B B\tau_e}{\hbar}\left(\frac{x-y}{y+z}\right)\right)^2$. The parallel field MR data has been tried to fit with Equation 4.12 and is shown in Figure 4.9(a). The fitted curve has deviations from the experimental data and is not capable of explaining the full range MR for low temperatures. The experimental data has a strong temperature dependency that is not captured in Equation 4.12, as only temperature dependency in the equation is coming from τ_ϕ ($\tau_\phi \sim T^{-1}$).

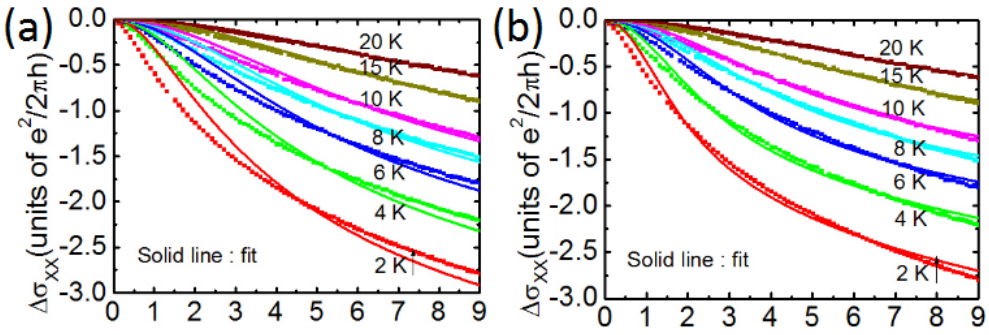

Figure 4.9: Zeeman effect and the EEI effect in parallel field MR (published in [74]): (a) The full range data are fitted by Maekawa and Fukuyama theory of localization for parallel field, fitting is not satisfactory. (b) The full range data fitted by the EEI theory of Lee and Ramakrishnan, fitting is better than fit in (a).

4.3.2 Electron Electron Interaction Effect

The single particle localization theory of Maekawa and Fukuyama is not enough to describe our data. We considered the EEI theory of Lee-Ramakrishnan [66] where the Zeeman contribution is taken into account via Hartree-Fock method. In the EEI

theory [66] Equation 4.9 gives the field dependence of the conductivity at a particular temperature, considering the Zeeman spin splitting,

$$\Delta\sigma_{EEI}(B,T) = -\frac{e^2}{4\pi^2\hbar}F_\sigma g_2(B,T) \tag{4.13}$$

where,

$$F_\sigma = -4 + \frac{8\left(1+\frac{F}{2}\right)\ln\left(1+\frac{F}{2}\right)}{F}, \tag{4.14}$$

with

$$F = \frac{\int_0^\infty d\Omega\ v(q = 2k_F\sin(\frac{\theta}{2}))}{\int_0^\infty d\Omega\ v(0)}. \tag{4.15}$$

Here, $v(q)$ is the Fourier transform of screened Coulomb potential and the integral is on the Fermi surface over the solid angle Ω. The function g_2 is given by [66],

$$g_2(B,T) = \int_0^\infty d\omega\ \ln\left|1-\left(\frac{g\mu_B B/k_B T}{\omega}\right)^2\right|\frac{d^2}{d\omega^2}\frac{\omega}{e^\omega-1}. \tag{4.16}$$

The parallel field MR data has been fitted with the EEI theory and is shown in Figure 4.9(b). The fitting using EEI theory is substantially better than the previous fit and has all the qualitative features of the original data. The temperature dependency of the experimental data can be understood from the EEI theory quite well. The fitting parameters obtained from the fitting are $F_\sigma = 0.94$, $g = 7.5$ at 2 K, which are in the range of previously obtained values [50, 51, 95, 96]. Still the fitted curve deviates from the original data as clearly visible in Figure 4.9(b).

In literature [50, 51], a combined model has been used where the contribution from localization and EEI have been added [74],

$$\Delta\sigma(B) = \Delta\sigma_L(B) + \Delta\sigma_{EEI}(B). \tag{4.17}$$

The fitting using the combined model have excellent agreement to our experimental data over the entire field range, which is shown in Figure 4.10(a). Although the expression for EEI neglects spin-orbit scattering for in-plane spin polarization, it serves as a very good approximation because $1/\tau_{SO_x}$ is very small [66]. The value of the fitting parameters, extracted from the $\Delta\sigma_{EEI}(B)$ contribution in the combined model fitting, are $F_\sigma = 0.66$, $g = 10$ at 2 K. The perpendicular field MR data fitting gives $l_\phi = 145$ nm and $l_e = 20.5$ nm, and using these values we obtained the ratio $(x - y)/(y + z)$ from the $\Delta\sigma_L(B)$ contribution in the combined model fitting. The ratio $(x-y)/(y+z)$ should be large due to strong SOC in Bi_2Te_3, instead we obtained a small value. Such small value of the ratio $(x - y)/(y + z)$ has been reported for Bi_2Se_3 [51] and is not well understood. From relative deviations in fitting shown in Figure 4.9(a) and Figure 4.9(b), it is clear that the contribution of the term $\Delta\sigma_L(B)$ is less than $\Delta\sigma_{EEI}(B)$, i.e the parallel field MR is mainly due to contribution from EEI. Such small contribution from the $\Delta\sigma_L(B)$ term may be the reason for such small value of the ratio $(x-y)/(y+z)$. That the contribution of EEI is mainly responsible for the parallel field MR is also clear from the fact that at high fields the slope from the logarithmic dependence of MR with field is $F_\sigma \sim 0.7$, as shown in Figure 4.8(b).

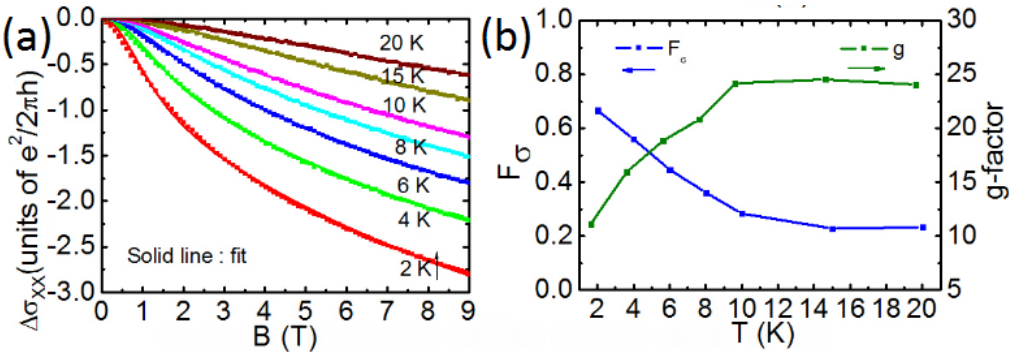

Figure 4.10: Combined model fit for entire parallel field MR (published in [74]): (a) Parallel field MR fitted by the combined model for entire field range. (b) The extracted F_σ and the g-factor are plotted versus temperature.

The Zeeman g-factor and strength of Coulomb interaction F_σ are extracted from the combined model fit and are plotted versus T in Figure 4.10(b). The extracted g-factor, in our case, is 10-25 over the 2-20 K range and matches well with previously reported values of g for Bi_2Se_3 and Bi_2Te_3 [95, 96]. From EEI theory, the condition that the parallel field MR will be parabolic for small fields, is $g\mu_B B < k_B T$ or $B < (k_B T/g\mu_B) \sim 0.3$ T for $T = 2$ K. The parabolic MR is valid up to 0.3 T field, and so we obtained a good B^2 fit for field up to 0.4 T, as shown in Figure 4.8(a). The reason that F_σ is increasing and the g-factor is decreasing with decreasing temperature is not clear. We have estimated F_σ from Equation 4.14 and Equation 4.15 to match it with our value. We first assumed a 3D screening, and to calculate the screened Coulomb potential we used the Thomas-Fermi approximation in 3D [97], where the Thomas-Fermi wave vector k_{TF} is given by,

$$k_{TF} = (m^* e^2 k_F / \epsilon \pi^2 \hbar^2)^{\frac{1}{2}}. \tag{4.18}$$

where ϵ is an effective permittivity for the TI and its surroundings. Here ϵ is taken to be that of free space because in our case the mean in-plane distance between electrons (order of k_F^{-1}) is in the same order as film thickness and most of the electric field lines pass through the surrounding media [98, 99]. In our case, the calculated Thomas-Fermi screening length (inverse of $k_{TF} \sim 5$ nm) is also comparable to the thickness, suggesting that in our thin film the screening is approaching 2D. The two cases for 2D electrons have been considered next: electrons in a parabolic conduction band, and electrons in a linear Dirac cone. For calculating screened Coulomb potential in 2D screening, Lindhard theory [100] have been used. Lindhard theory gives [100],

$$v(q) = (2\pi e^2/\epsilon)(1/(q + k_0)), \tag{4.19}$$

where k_0 is the screening wave vector. For parabolic dispersion, the theory [100] gives

$$k_0 = (m^* e^2 / 2\epsilon\pi\hbar^2) \tag{4.20}$$

and for linear dispersion the theory [100] gives

$$k_0 = (e^2 k_F / 2\epsilon\pi\hbar v_F). \tag{4.21}$$

For parabolic dispersion, assuming $\varepsilon_F = 0.58$ eV lying 0.28 eV above the assumed band edge, we obtain $F = 0.81$ and $F_\sigma = 0.72$ at 2 K. For linear dispersion, at 2 K we obtain $F = 0.89$, $F_\sigma = 0.78$ irrespective of Fermi energy ε_F. Given the various approximations, these numbers perhaps are not substantially different. The value obtained at 2 K from the data fitting in Figure 4.10(a) is $F_\sigma = 0.66$, is comparable to these calculated values, and to other reported experimental values [50, 51].

4.4 Angle Dependent Anisotropic Magnetoresistance

In Figure 4.7(b), we have observed that for field orientation less than 75°, the MR shows very little deviations from no tilt case. The Zeeman effect and the EEI effect are suppressed in perpendicular field MR due to strong SOC and change in perpendicular field MR can be described by HLN theory alone. The Zeeman effect and the EEI effect are significant in MR only when the field is near parallel. We have observed the angular dependence of magnetoconductivity as shown in Figure 4.11. Figure 4.11 shows magnetoconductivity versus θ (the angle between the magnetic field and the surface normal) for different temperatures and different field values.

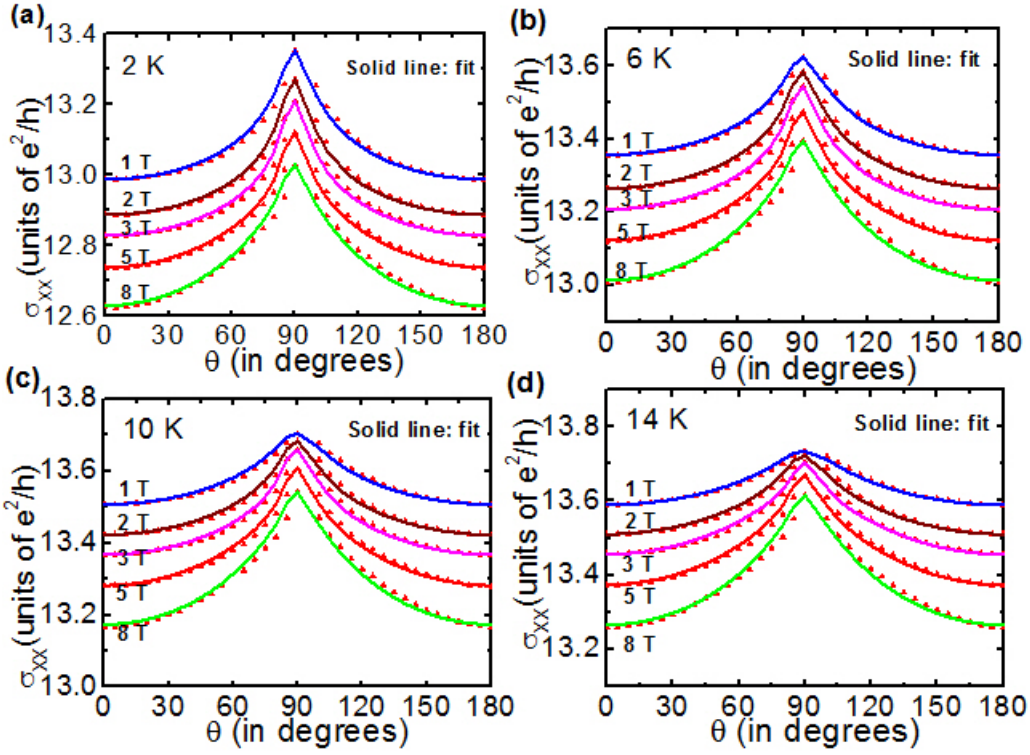

Figure 4.11: Anisotropic MR for different fields and different temperatures (published in [74]): The MR is plotted with different field orientations for different field value and different temperatures (a) - (d). The MR shows anisotropy with respect the field direction. The data is fitted with the original HLN equation and the fitting is satisfactory.

The magnetoconductivity shows anisotropy with respect to the field direction. This anisotropy is mainly because the perpendicular component of the magnetic field is responsible for suppressing the WAL effect and causing a change in conductivity as the field component varies with angle. To fit the data accordingly, we have used [74]

$$\Delta\sigma(B\cos\theta) = \sigma(B\cos\theta) - \sigma(B\cos(\theta = 90^\circ)), \tag{4.22}$$

and replaced the $\sigma(B, \theta = 90^\circ)$ data-point by $\sigma(B = 0)$, as the change in MR for parallel field is due to the Zeeman effect and that effect is not taken care in HLN theory.

Figure 4.11 shows fitting of the experimental data with the original HLN Equation, Equation 4.3. We found that HLN theory can describe the angular dependency quite well. The small anomalies in fitting at angles near 90° is due to the Zeeman effect.

5

Thesis summary

This thesis presents detailed magneto-transport studies of epitaxially grown Bi_2Te_3 topological insulator thin films on Si(111), with magnetic field parallel and perpendicular to the sample surface. Methods of growing the film by molecular beam epitaxy, and characterizing the grown film by reflection high energy electron diffraction, scanning tunnelling microscopy, x-ray photoelectron spectroscopy and x-ray diffraction have been presented. The quality and the crystallinity of the films reported here are very good, despite a large lattice mismatch between the film and the substrate. This molecular beam epitaxy grown topological insulator film will be useful for integration with Si technology for further device application. The parallel and perpendicular field magnetoresistance data have been analyzed with existing theory, which gives information about useful charge and spin transport parameters. The perpendicular field MR data has been explained with the original Hikami-Larkin-Nagaoka theory, which suggest weak antilocalization in the thin film. The Zeeman effect is found to be suppressed in the perpendicular field magnetoresistance due to the presence of strong spin orbit coupling in the thin films. The parallel field magnetoresistance data has been explained with the combination of the localization theory of Maekawa-

Fukuyama and the electron-electron interaction theory of Lee-Ramakrishnan, considering Zeeman spin splitting effect in both the theory. The magnetoresistance exhibits anisotropy with respect to the field direction. A large spin-orbit relaxation time for spin polarization parallel to the plane and a small spin-orbit relaxation time for spin polarization normal to the plane have been found. The large spin-orbit relaxation time for spin polarization parallel to the plane leads to Zeeman spin splitting contributions in parallel field magnetoresistance, while the small spin-orbit relaxation time for spin polarization normal to the plane leads to suppression of that in perpendicular field magnetoresistance. The phase coherence length, the mean free path, the Zeeman g-factor and the strength of Coulomb screening also have been estimated. The estimation of these charge and spin transport parameters are useful considering spintronics application of topological insulator magneto-electric devices. Further comparison of these parameters can be performed for different topological insulator materials with different type of magnetic and non-magnetic impurity doping. Also the angle-dependent anisotropy of magnetoresistance can be used in anisotropic magnetic sensor applications.

Bibliography

[1] J. E. Moore, "Topological insulators: The next generation," *Nature Physics*, vol. 5, no. 6, pp. 378–380, 2009.

[2] J. E. Moore, "The birth of topological insulators.," *Nature*, vol. 464, no. 7286, pp. 194–198, 2010.

[3] X.-L. Qi and S.-C. Zhang, "The quantum spin Hall effect and topological insulators," *Physics Today*, vol. 63, no. 1, p. 33, 2010.

[4] M. Z. Hasan and C. L. Kane, "*Colloquium* : Topological insulators," *Rev. Mod. Phys.*, vol. 82, pp. 3045–3067, November 2010.

[5] X.-L. Qi and S.-C. Zhang, "Topological insulators and superconductors," *Rev. Mod. Phys.*, vol. 83, pp. 1057–1110, October 2011.

[6] Y. Xia, D. Qian, D. Hsieh, L. Wray, A. Pal, H. Lin, A. Bansil, D. Grauer, Y. S. Hor, R. J. Cava, and M. Z. Hasan, "Observation of a large-gap topological-insulator class with a single Dirac cone on the surface," *Nature Physics*, vol. 5, pp. 398–402, May 2009.

[7] H. Zhang, C.-X. Liu, X.-L. Qi, X. Dai, Z. Fang, and S.-C. Zhang, "Topological insulators in Bi_2Se_3, Bi_2Te_3 and Sb_2Te_3 with a single Dirac cone on the surface," *Nature Physics*, vol. 5, pp. 438–442, May 2009.

[8] L. Fu, C. L. Kane, and E. J. Mele, "Topological insulators in three dimensions," *Phys. Rev. Lett.*, vol. 98, p. 106803, March 2007.

[9] D. Hsieh, D. Qian, L. Wray, Y. Xia, Y. S. Hor, R. J. Cava, and M. Z. Hasan, "A topological Dirac insulator in a quantum spin Hall phase.," *Nature*, vol. 452, no. 7190, pp. 970–4, 2008.

[10] L. Fu and C. L. Kane, "Superconducting proximity effect and Majorana fermions at the surface of a topological insulator," *Phys. Rev. Lett.*, vol. 100, p. 096407, March 2008.

[11] X.-L. Qi, R. Li, J. Zang, and S.-C. Zhang, "Inducing a magnetic monopole with topological surface states," *Science*, vol. 323, pp. 1184–1187, February 2009.

[12] P. Roushan, J. Seo, C. V. Parker, Y. S. Hor, D. Hsieh, D. Qian, A. Richardella, M. Z. Hasan, R. J. Cava, and A. Yazdani, "Topological surface states protected from backscattering by chiral spin texture.," *Nature*, vol. 460, no. 7259, pp. 1106–1109, 2009.

[13] Y.-L. Chen, J.-G. Analytis, J.-H. Chu, Z.-K. Liu, S.-K. Mo, X.-L. Qi, H.-J. Zhang, D.-H. Lu, X. Dai, Z. Fang, S.-C. Zhang, I.-R. Fisher, Z. Hussain, and Z.-X. Shen, "Experimental realization of a three-dimensional topological insulator, Bi_2Te_3.," *Science*, vol. 325, no. 5937, pp. 178–181, 2009.

[14] D. Hsieh, Y. Xia, L. Wray, D. Qian, A. Pal, J. H. Dil, J. Osterwalder, F. Meier, G. Bihlmayer, C. L. Kane, Y. S. Hor, R. J. Cava, and M. Z. Hasan, "Observation of unconventional quantum spin textures in topological insulators.," *Science*, vol. 323, no. 5916, pp. 919–922, 2009.

[15] H. Peng, K. Lai, D. Kong, S. Meister, Y. Chen, X.-L. Qi, S.-C. Zhang, Z.-X. Shen, and Y. Cui, "Aharonov-Bohm interference in topological insulator nanoribbons.," *Nature materials*, vol. 9, no. 3, pp. 225–229, 2010.

[16] G. S. Nolan, J. Sharp, and G. H. J., *Thermoelectric: Basic Principles and New Materials Developments*. Springer, New York, 2001.

[17] Y. Ando, "Topological insulator materials," *Journal of the Physical Society of Japan*, vol. 82, no. 10, p. 102001, 2013.

[18] Z. Li and J. P. Carbotte, "Hexagonal warping on optical conductivity of surface states in topological insulator Bi_2Te_3," *Phys. Rev. B*, vol. 87, p. 155416, April 2013.

[19] P. Ghaemi, R. S. K. Mong, and J. E. Moore, "In-plane transport and enhanced thermoelectric performance in thin films of the topological insulators Bi_2Se_3 and Bi_2Te_3," *Phys. Rev. Lett.*, vol. 105, p. 166603, October 2010.

[20] C.-X. Liu, H. Zhang, B. Yan, X.-L. Qi, T. Frauenheim, X. Dai, Z. Fang, and S.-C. Zhang, "Oscillatory crossover from two-dimensional to three-dimensional topological insulators," *Phys. Rev. B*, vol. 81, p. 041307, January 2010.

[21] H.-Z. Lu, W.-Y. Shan, W. Yao, Q. Niu, and S.-Q. Shen, "Massive Dirac fermions and spin physics in an ultrathin film of topological insulator," *Phys. Rev. B*, vol. 81, p. 115407, March 2010.

[22] K. He, Y. Zhang, C.-Z. Chang, C.-L. Song, L.-L. Wang, X. Chen, J.-F. Jia, Z. Fang, X. Dai, W.-Y. Shan, S.-Q. Shen, Q. Niu, X.-L. Qi, S.-C. Zhang, X.-C. Ma, and Q.-K. Xue, "Crossover of the three-dimensional topological insulator Bi_2Se_3 to the two-dimensional limit," *Nature Physics*, vol. 6, no. 8, pp. 584–588, 2010.

[23] K. Park, J. J. Heremans, V. W. Scarola, and D. Minic, "Robustness of topologically protected surface states in layering of Bi_2Te_3 thin films," *Phys. Rev. Lett.*, vol. 105, p. 186801, October 2010.

[24] Y.-Y. Li, G. Wang, X.-G. Zhu, M.-H. Liu, C. Ye, X. Chen, Y.-Y. Wang, K. He, L.-L. Wang, X.-C. Ma, H.-J. Zhang, X. Dai, Z. Fang, X.-C. Xie, Y. Liu, X.-L. Qi, J.-F. Jia, S.-C. Zhang, and Q.-K. Xue, "Intrinsic topological insulator Bi_2Te_3 thin films on Si and their thickness limit.," *Advanced materials*, vol. 22, no. 36, pp. 4002–4007, 2010.

[25] Y. Liu, G. Bian, T. Miller, M. Bissen, and T.-C. Chiang, "Topological limit of ultrathin quasi-free-standing Bi_2Te_3 films grown on Si(111)," *Phys. Rev. B*, vol. 85, p. 195442, May 2012.

[26] A. A. Taskin, S. Sasaki, K. Segawa, and Y. Ando, "Manifestation of topological protection in transport properties of epitaxial Bi_2Se_3 thin films," *Phys. Rev. Lett.*, vol. 109, p. 066803, August 2012.

[27] H. Steinberg, J.-B. Laloë, V. Fatemi, J. S. Moodera, and P. Jarillo-Herrero, "Electrically tunable surface-to-bulk coherent coupling in topological insulator thin films," *Phys. Rev. B*, vol. 84, p. 233101, December 2011.

[28] H.-Z. Lu, J. Shi, and S.-Q. Shen, "Competition between weak localization and antilocalization in topological surface states," *Phys. Rev. Lett.*, vol. 107, p. 076801, August 2011.

[29] D. Teweldebrhan, V. Goyal, and A. A. Balandin, "Exfoliation and characterization of bismuth telluride atomic quintuples and quasi-two-dimensional crystals," *Nano Letters*, vol. 10, no. 4, pp. 1209–1218, 2010.

[30] K. M. F. Shahil, M. Z. Hossain, V. Goyal, and A. A. Balandin, "Micro-Raman spectroscopy of mechanically exfoliated few-quintuple layers of Bi_2Te_3, Bi_2Se_3, and Sb_2Te_3 materials," *Journal of Applied Physics*, vol. 111, no. 5, p. 054305, 2012.

[31] D. Teweldebrhan, V. Goyal, M. Rahman, and A. A. Balandin, "Atomically-thin crystalline films and ribbons of bismuth telluride," *Applied Physics Letters*, vol. 96, no. 5, p. 053107, 2010.

[32] X. Liu, D. J. Smith, J. Fan, Y.-H. Zhang, H. Cao, Y. P. Chen, J. Leiner, B. J. Kirby, M. Dobrowolska, and J. K. Furdyna, "Structural properties of Bi_2Te_3 and Bi_2Se_3 topological insulators grown by molecular beam epitaxy on GaAs(001) substrates," *Applied Physics Letters*, vol. 99, no. 17, p. 171903, 2011.

[33] X. Yu, L. He, M. Lang, W. Jiang, F. Xiu, Z. Liao, Y. Wang, X. Kou, P. Zhang, J. Tang, G. Huang, J. Zou, and K. L. Wang, "Separation of top and bottom surface conduction in Bi_2Te_3 thin films," *Nanotechnology*, vol. 24, no. 1, p. 015705, 2013.

[34] J. J. Lee, F. T. Schmitt, R. G. Moore, I. M. Vishik, Y. Ma, and Z. X. Shen, "Intrinsic ultrathin topological insulators grown via molecular beam epitaxy characterized by in-situ angle resolved photoemission spectroscopy," *Applied Physics Letters*, vol. 101, no. 1, p. 013118, 2012.

[35] G. Zhang, H. Qin, J. Chen, X. He, L. Lu, Y. Li, and K. Wu, "Growth of topological insulator Bi_2Se_3 thin films on $SrTiO_3$ with large tunability in chemical potential," *Advanced Functional Materials*, vol. 21, no. 12, pp. 2351–2355, 2011.

[36] J. Park, Y.-A. Soh, G. Aeppli, S. R. Bland, X.-G. Zhu, X. Chen, Q.-K. Xue, and F. Grey, "Crystal structure and epitaxy of Bi_2Te_3 films grown on Si," *Applied Physics Letters*, vol. 101, no. 22, p. 221910, 2012.

[37] H. W. Liu, H. T. Yuan, N. Fukui, L. Zhang, J. F. Jia, Y. Iwasa, M. W. Chen, T. Hashizume, T. Sakurai, and Q. K. Xue, "Growth of topological insulator Bi_2Te_3 ultrathin films on Si(111) investigated by low-energy electron microscopy," *Crystal Growth and Design*, vol. 10, no. 10, pp. 4491–4493, 2010.

[38] J. Krumrain, G. Mussler, S. Borisova, T. Stoica, L. Plucinski, C. Schneider, and D. Grtzmacher, "MBE growth optimization of topological insulator Bi_2Te_3 films," *Journal of Crystal Growth*, vol. 324, no. 1, pp. 115–118, 2011.

[39] H. Cao, R. Venkatasubramanian, C. Liu, J. Pierce, H. Yang, M. Zahid Hasan, Y. Wu, and Y. P. Chen, "Topological insulator Bi_2Te_3 films synthesized by metal organic chemical vapor deposition," *Applied Physics Letters*, vol. 101, no. 16, p. 162104, 2012.

[40] L. D. Alegria and J. R. Petta, "Controlled MOCVD growth of Bi_2Se_3 topological insulator nanoribbons," *Nanotechnology*, vol. 23, no. 43, p. 435601, 2012.

[41] F. Xiu, L. He, Y. Wang, L. Cheng, L.-T. Chang, M. Lang, G. Huang, X. Kou, Y. Zhou, X. Jiang, Z. Chen, J. Zou, A. Shailos, and K. L. Wang, "Manipulating surface states in topological insulator nanoribbons.," *Nature nanotechnology*, vol. 6, no. 4, pp. 216–221, 2011.

[42] D.-X. Qu, Y. S. Hor, J. Xiong, R. J. Cava, and N. P. Ong, "Quantum oscillations and hall anomaly of surface states in the topological insulator Bi_2Te_3.," *Science*, vol. 329, no. 5993, pp. 821–824, 2010.

[43] Z. Ren, A. A. Taskin, S. Sasaki, K. Segawa, and Y. Ando, "Large bulk resistivity and surface quantum oscillations in the topological insulator Bi_2Te_2Se," *Phys. Rev. B*, vol. 82, p. 241306, December 2010.

[44] J. G. Checkelsky, Y. S. Hor, M.-H. Liu, D.-X. Qu, R. J. Cava, and N. P. Ong, "Quantum Interference in Macroscopic Crystals of Nonmetallic Bi_2Se_3," *Phys. Rev. Lett.*, vol. 103, p. 246601, December 2009.

[45] Z. Li, T. Chen, H. Pan, F. Song, B. Wang, J. Han, Y. Qin, X. Wang, R. Zhang, J. Wan, D. Xing, and G. Wang, "Two-dimensional universal conductance fluctuations and the electron-phonon interaction of surface states in Bi_2Te_2Se microflakes.," *Scientific reports*, vol. 2, p. 595, 2012.

[46] J. Chen, H. J. Qin, F. Yang, J. Liu, T. Guan, F. M. Qu, G. H. Zhang, J. R. Shi, X. C. Xie, C. L. Yang, K. H. Wu, Y. Q. Li, and L. Lu, "Gate-voltage control of chemical potential and weak antilocalization in Bi_2Se_3," *Phys. Rev. Lett.*, vol. 105, p. 176602, October 2010.

[47] J. G. Checkelsky, Y. S. Hor, R. J. Cava, and N. P. Ong, "Bulk band gap and surface state conduction observed in voltage-tuned crystals of the topological insulator Bi_2Se_3," *Phys. Rev. Lett.*, vol. 106, p. 196801, May 2011.

[48] H.-T. He, G. Wang, T. Zhang, I.-K. Sou, G. K. L. Wong, J.-N. Wang, H.-Z. Lu, S.-Q. Shen, and F.-C. Zhang, "Impurity effect on weak antilocalization in the topological insulator Bi_2Te_3," *Phys. Rev. Lett.*, vol. 106, p. 166805, April 2011.

[49] J. Chen, X. Y. He, K. H. Wu, Z. Q. Ji, L. Lu, J. R. Shi, J. H. Smet, and Y. Q. Li, "Tunable surface conductivity in Bi_2Se_3 revealed in diffusive electron transport," *Phys. Rev. B*, vol. 83, p. 241304, June 2011.

[50] M. Liu, C.-Z. Chang, Z. Zhang, Y. Zhang, W. Ruan, K. He, L.-L. Wang, X. Chen, J.-F. Jia, S.-C. Zhang, Q.-K. Xue, X. Ma, and Y. Wang, "Electron interaction-driven insulating ground state in Bi_2Se_3 topological insulators in the two-dimensional limit," *Phys. Rev. B*, vol. 83, p. 165440, April 2011.

[51] J. Wang, A. M. DaSilva, C.-Z. Chang, K. He, J. K. Jain, N. Samarth, X.-C. Ma, Q.-K. Xue, and M. H. W. Chan, "Evidence for electron-electron interaction in topological insulator thin films," *Phys. Rev. B*, vol. 83, p. 245438, June 2011.

[52] Y. S. Kim, M. Brahlek, N. Bansal, E. Edrey, G. A. Kapilevich, K. Iida, M. Tanimura, Y. Horibe, S.-W. Cheong, and S. Oh, "Thickness-dependent bulk properties and weak antilocalization effect in topological insulator Bi_2Se_3," *Phys. Rev. B*, vol. 84, p. 073109, August 2011.

[53] Y. Takagaki, B. Jenichen, U. Jahn, M. Ramsteiner, and K.-J. Friedland, "Weak antilocalization and electron-electron interaction effects in Cu-doped Bi_2Se_3 films," *Phys. Rev. B*, vol. 85, p. 115314, March 2012.

[54] S.-P. Chiu and J.-J. Lin, "Weak antilocalization in topological insulator Bi_2Te_3 microflakes," *Phys. Rev. B*, vol. 87, p. 035122, January 2013.

[55] H. Cao, J. Tian, I. Miotkowski, T. Shen, J. Hu, S. Qiao, and Y. P. Chen, "Quantized Hall effect and Shubnikov de Haas oscillations in highly doped Bi_2Se_3: Evidence for layered transport of bulk carriers," *Phys. Rev. Lett.*, vol. 108, p. 216803, May 2012.

[56] T. Zhang, P. Cheng, X. Chen, J.-F. Jia, X. Ma, K. He, L. Wang, H. Zhang, X. Dai, Z. Fang, X. Xie, and Q.-K. Xue, "Experimental demonstration of topological surface states protected by time-reversal symmetry," *Phys. Rev. Lett.*, vol. 103, p. 266803, December 2009.

[57] P. M. Ostrovsky, I. V. Gornyi, and A. D. Mirlin, "Interaction-induced criticality in Z_2 topological insulators," *Phys. Rev. Lett.*, vol. 105, p. 036803, July 2010.

[58] K. Nomura, M. Koshino, and S. Ryu, "Topological delocalization of two-dimensional massless Dirac fermions," *Phys. Rev. Lett.*, vol. 99, p. 146806, October 2007.

[59] G. Bergmann, "Weak localization in thin films: A time-of-flight experiment with conduction electrons," *Phys. Rep.*, vol. 107, pp. 1–58, 1984.

[60] S. Kobayashi and F. Komori, "Experiments on localization and interaction effects in metallic films," *Prog. Theor. Phys. Supplement*, vol. 84, pp. 224–248, 1985.

[61] G. Zhang, H. Qin, J. Chen, X. He, L. Lu, Y. Li, and K. Wu, "Growth of topological insulator Bi_2Se_3 thin films on SrTiO3 with large tunability in chemical potential," *Advanced Functional Materials*, vol. 21, pp. 2351–2355, June 2011.

[62] J. H. Bardarson, J. Tworzydło, P. W. Brouwer, and C. W. J. Beenakker, "One-parameter scaling at the Dirac point in graphene," *Phys. Rev. Lett.*, vol. 99, p. 106801, September 2007.

[63] K. Nomura, M. Koshino, and S. Ryu, "Topological delocalization of two-dimensional massless Dirac fermions," *Phys. Rev. Lett.*, vol. 99, p. 146806, October 2007.

[64] S. Hikami, A. Larkin, and Y. Nagaoka, "Spin-orbit interaction and magnetoresistance in the two dimensional random system," *Progress of Theoretical Physics*, vol. 63, no. 2, pp. 707–710, 1980.

[65] S. Maekawa and H. Fukuyama, "Magnetoresistance in two-dimensional disordered systems: Effects of Zeeman splitting and spin-orbit scattering," *Journal of the Physical Society of Japan*, vol. 50, no. 8, pp. 2516–2524, 1981.

[66] P. A. Lee and T. V. Ramakrishnan, "Disordered electronic systems," *Rev. Mod. Phys.*, vol. 57, pp. 287–337, April 1985.

[67] M. A. Herman, W. Richter, and H. Sitter, *Epitaxy: Physical Principles and Technical Implementation*. Springer-Verlag, 2003.

[68] A. Roy, *Aspects Of Self-Assembled Nanostructures Grown By Molecular Beam Epitaxy On Pristine, Ion-Beam Modified And Oxidized Silicon Surfaces*. PhD Dissertation, Jadavpur University, 2011.

[69] W. S. Knodle, C. R., and K. Seshan, *Handbook of Thin Film Deposition Proccesses and Technology*. Noyes Publications/William Andrew Publishing, 2002.

[70] K. Oura, V. G. Lifshits, A. A. Saranin, A. V. Zotov, and M. Katayama, *Surface Science - An Introduction*. Springer-Verlag, 2003.

[71] A. Koma, "Van der Waals epitaxy for highly lattice-mismatched systems," *Journal of Crystal Growth*, vol. 201-202, pp. 236–241, May 1999.

[72] A. Roy, S. Guchhait, S. Sonde, R. Dey, T. Pramanik, A. Rai, H. C. P. Movva, L. Colombo, and S. K. Banerjee, "Two-dimensional weak anti-localization in Bi_2Te_3 thin film grown on Si(111)-(7×7) surface by molecular beam epitaxy," *Applied Physics Letters*, vol. 102, no. 16, p. 163118, 2013.

[73] J. P. A. v. d. Wagt, *Reflection High Energy Electron Diffraction During Molecular Beam Epitaxy*. PhD Dissertation, Stanford University, 1994.

[74] R. Dey, T. Pramanik, A. Roy, A. Rai, S. Guchhait, S. Sonde, H. C. P. Movva, L. Colombo, L. F. Register, and S. K. Banerjee, "Strong spin-orbit coupling and Zeeman spin splitting in angle dependent magnetoresistance of Bi_2Te_3," *Applied Physics Letters*, vol. 104, no. 22, p. 223111, 2014.

[75] M. Lang, L. He, X. Kou, P. Upadhyaya, Y. Fan, H. Chu, Y. Jiang, J. H. Bardarson, W. Jiang, E. S. Choi, Y. Wang, N.-C. Yeh, J. Moore, and K. L. Wang, "Competing weak localization and weak antilocalization in ultrathin topological insulators," *Nano Letters*, vol. 13, no. 1, pp. 48–53, 2013.

[76] B. Y. Yavorsky, N. F. Hinsche, I. Mertig, and P. Zahn, "Electronic structure and transport anisotropy of Bi_2Te_3 and Sb_2Te_3," *Phys. Rev. B*, vol. 84, p. 165208, October 2011.

[77] R. L. Kallaher and J. J. Heremans, "Spin and phase coherence measured by antilocalization in n-InSb thin films," *Physical Review B*, vol. 79, p. 075322, Feb 2009.

[78] J. Rammer and A. Schmid, "Destruction of phase coherence by electron-phonon interactions in disordered conductors," *Physical Review B*, vol. 34, pp. 1352–1355, Jul 1986.

[79] H. Tang, D. Liang, R. L. J. Qiu, and X. P. A. Gao, "Two-dimensional transport-induced linear magneto-resistance in topological insulator Bi_2Se_3 nanoribbons," *ACS Nano*, vol. 5, no. 9, pp. 7510–7516, 2011.

[80] H. He, B. Li, H. Liu, X. Guo, Z. Wang, M. Xie, and J. Wang, "High-field linear magneto-resistance in topological insulator Bi_2Se_3 thin films," *Applied Physics Letters*, vol. 100, no. 3, p. 032105, 2012.

[81] A. A. Abrikosov, "Quantum magnetoresistance," *Phys. Rev. B*, vol. 58, pp. 2788–2794, August 1998.

[82] H. B. Zhang, H. L. Yu, D. H. Bao, S. W. Li, C. X. Wang, and G. W. Yang, "Weak localization bulk state in a topological insulator Bi_2Te_3 film," *Phys. Rev. B*, vol. 86, p. 075102, August 2012.

[83] H.-Z. Lu and S.-Q. Shen, "Weak localization of bulk channels in topological insulator thin films," *Phys. Rev. B*, vol. 84, p. 125138, September 2011.

[84] I. Garate and L. Glazman, "Weak localization and antilocalization in topological insulator thin films with coherent bulk-surface coupling," *Phys. Rev. B*, vol. 86, p. 035422, July 2012.

[85] B. A. Bernevig, T. L. Hughes, and S.-C. Zhang, "Quantum spin Hall effect and topological phase transition in HgTe quantum wells," *Science*, vol. 314, no. 5806, pp. 1757–1761, 2006.

[86] M. Knig, S. Wiedmann, C. Brne, A. Roth, H. Buhmann, L. W. Molenkamp, X.-L. Qi, and S.-C. Zhang, "Quantum spin Hall insulator state in HgTe quantum wells," *Science*, vol. 318, no. 5851, pp. 766–770, 2007.

[87] S. X. Zhang, R. D. McDonald, A. Shekhter, Z. X. Bi, Y. Li, Q. X. Jia, and S. T. Picraux, "Magneto-resistance up to 60 Tesla in topological insulator Bi_2Te_3 thin films," *Applied Physics Letters*, vol. 101, no. 20, p. 202403, 2012.

[88] D. Pesin and A. H. MacDonald, "Spintronics and pseudospintronics in graphene and topological insulators.," *Nature materials*, vol. 11, pp. 409–16, May 2012.

[89] A. A. Burkov and D. G. Hawthorn, "Spin and charge transport on the surface of a topological insulator," *Phys. Rev. Lett.*, vol. 105, p. 066802, August 2010.

[90] D. Kowal, M. Ben-Chorin, and Z. Ovadyahu, "Effects of Zeeman splitting on weak antilocalization," *Phys. Rev. B*, vol. 44, pp. 9080–9083, October 1991.

[91] A. Sahnoune, J. O. Ström-Olsen, and H. E. Fischer, "Influence of spin-orbit scattering on the magnetoresistance due to enhanced electron-electron interactions," *Phys. Rev. B*, vol. 46, pp. 10035–10040, October 1992.

[92] A. J. Millis and P. A. Lee, "Spin-orbit and paramagnon effects on magnetoconductance and tunneling," *Phys. Rev. B*, vol. 30, pp. 6170–6173, November 1984.

[93] Y. Lyanda-Geller, "Quantum interference and electron-electron interactions at strong spin-orbit coupling in disordered systems," *Phys. Rev. Lett.*, vol. 80, pp. 4273–4276, May 1998.

[94] X. Wang, X. He, T. Guan, J. Liao, C. Lin, K. Wu, Y. Li, and C. Zeng, "Transport properties of topological insulator Bi_2Se_3 thin films in tilted magnetic fields," *Physica E: Low-dimensional Systems and Nanostructures*, vol. 46, pp. 236–240, 2012.

[95] H. Khler and E. Wchner, "The g-factor of the conduction electrons in Bi_2Se_3," *Physica Status Solidi (b)*, vol. 67, no. 2, pp. 665–675, 1975.

[96] H. Khler, "Anisotropic g-Factor of the conduction electrons in Bi_2Te_3," *Physica Status Solidi (b)*, vol. 75, no. 1, pp. 127–136, 1976.

[97] N. W. Ashcroft and N. D. Mermin, *Solid State Physics*. 1976.

[98] D. K. Efimkin, Y. E. Lozovik, and A. A. Sokolik, "Electron-hole pairing in a topological insulator thin film," *Phys. Rev. B*, vol. 86, p. 115436, September 2012.

[99] D. Tilahun, B. Lee, E. M. Hankiewicz, and A. H. MacDonald, "Quantum Hall superfluids in topological insulator thin films," *Phys. Rev. Lett.*, vol. 107, p. 246401, December 2011.

[100] J. Lindhard *K. Dan. Vidensk. Selsk. Mat. Fys. Medd.*, vol. 28, pp. 8–10, 1954.